IEEE Access
Multidisciplinary ⋮ Rapid Review ⋮ Open Access Journal

Received April 8, 2021, accepted April 25, 2021, date of publication April 30, 2021, date of current version May 10, 2021.

Digital Object Identifier 10.1109/ACCESS.2021.3076913

Fabry-Perot Antenna Employing Artificial Magnetic Conductors and Phase Gradient Metasurface for Wideband Monostatic RCS Reduction and High Gain Tilted Beam Radiation

HASSAN UMAIR[1], TARIK BIN ABDUL LATEF[1], YOSHIHIDE YAMADA[2], TAYYAB HASSAN[3], WAN NOR LIZA BINTI WAN MAHADI[1], MOHAMADARIFF OTHMAN[1], KAMILIA KAMARDIN[2], (Senior Member, IEEE), AND MOUSA I. HUSSEIN[4]

[1]Department of Electrical Engineering, University of Malaya, Kuala Lumpur 50603, Malaysia
[2]Malaysia-Japan International Institute of Technology (MJIIT), Universiti Teknologi Malaysia, Kuala Lumpur 54100, Malaysia
[3]Centre of Excellence in Science and Applied Technologies (CESAT), Islamabad 44000, Pakistan
[4]Department of Electrical Engineering, United Arab Emirates University, Al Ain, United Arab Emirates

Corresponding author: Tarik Bin Abdul Latef (tariqlatef@um.edu.my)

This work was supported in part by the University of Malaya under Grant GPF015A-2019.

ABSTRACT Platforms with low radar signatures require compatible antennas (low scattering) for communication purposes. Under this context, the article presents two Fabry-Perot (FP) Cavity antennas (Ant-1 and Ant-2). Ant-1's aperture is an integrated design of artificial magnetic conductor (AMC) surface and a phase gradient metasurface (PGM), incorporating three unit-cell structures. The antenna achieves reduced monostatic scattering over broad bandwidth, and simultaneously obtains high gain as well as tilted beam peak radiation. Patch radiating at 7 GHz forms excitation source of the cavity, and cavity height is 0.33λ, smaller than the heights of conventional cavity designs (λ/2). RCS reduction is obtained over a bandwidth of 105.8% (4-13 GHz) for arbitrary polarizations, covering C/X bands. Antenna gain is 12 dB, and peak radiation tilt is −60° in elevation plane. Simulations have been verified through fabricated prototype. Ant-2 is a modification of Ant-1. Ant-2's aperture is constructed from two unit-cell structures, and its aperture size is 41% smaller than Ant-1. Its cavity height is 0.3λ. Ant-2 also achieves wideband backscattering reduction; however, due to asymmetric layout of unit-cell elements over the aperture, radar cross section (RCS) reduction bandwidth is different for the two polarizations. For vertically polarized (VP) incident wave, RCS reduction bandwidth is 105.8% (4-13 GHz), but for horizontally polarized (HP) wave, it is 85.7% (5.2-13 GHz). Nevertheless, broadband RCS reduction is still achieved for both polarizations. Peak gain is 11.73 dB, achieved at −37° tilt angle. Simulations are presented for Ant-2. Compared to literature, both antennas show various improved results.

INDEX TERMS Artificial magnetic conductor (AMC), Fabry-Perot (FP) cavity antenna, phase gradient metasurface (PGM), radar cross section (RCS), tilted beam radiation.

I. INTRODUCTION

With the rapid development in stealth technology, it is becoming increasingly important to develop antennas compatible with low radar cross section (RCS) platforms. Antennas can backscatter large amounts of radar waves and can enhance the likeliness of a stealth target to be captured on a radar [1], [2].

The associate editor coordinating the review of this manuscript and approving it for publication was Chan Hwang See.

To outdo this, several techniques have been employed for RCS reduction of antennas.

A prime factor to determine the suitability of a technique to be adopted for lowering the RCS of antenna depends on how it affects the antenna's radiation performance. It is desired that the antenna's performance remains unaffected/intact, while RCS reduction is achieved over a wideband (in-band + out-of-band frequencies). To achieve this, artificially engineered surfaces, generally known as metasurfaces, have

attracted a lot of attention, owing to their low profile and cost; ease of design and fabrication; and above all, offering the increased flexibility to engineer their electromagnetic (EM) response [3]. To this end, frequency selective surface (FSS) radomes [4] or ground planes [5], resistive electromagnetic band gap surfaces [6], and metamaterial absorbers [7], [8] have been implemented. In all of these implementations, either the RCS reduction bandwidth only covers out-of-band frequencies, it is narrow, or the antenna gain suffers.

Not only the wideband RCS reduction is important, but enhancing the antenna gain is also desired. In this regard, the use of metasurfaces with Fabry-Perot (FP) antenna configuration has been widely investigated [9]–[12]. Primarily, a patch antenna acts as the excitation source, and a specially designed superstrate forms an F-P cavity in conjunction with a perfectly conducting ground plane of the patch. A resistive FSS surface is etched on top side of the superstrate, backed by a partially reflecting surface (PRS) etched on its bottom side. In the antenna transmission mode, the radiated wave undergoes multiple reflections and transmissions between PRS and ground plane, finally emanating out with enhanced gain. In the reception mode, the resistive FSS in conjunction with the backing PRS acts like a conventional wideband resistive absorber [13], and most of the incident wave is dissipated as heat on its surface. It is important to note that since the whole superstrate is a passive structure, its transmission response is identical irrespective of whether the wave is being radiated or received, and therefore, does not disrupt the transmit/receive operation of the antenna. In [9], a metallic square loop with lumped resistors and a metallic plane with three parallel slots form the unit-cell of the superstrate. Wideband RCS reduction over 6-14 GHz has been achieved, along with broadside gain enhancement of 6.5 dB. In [10], the superstrate is slightly different, in that, the PRS part consists of periodic square slots. 8-14 GHz of RCS reduction bandwidth and about 7 dB of broadside gain increase has been reported. For frequency reconfiguration, phase tunable cells have been implemented above the ground plane to achieve frequency tuning from 9.05 to 10 GHz. In [11], the PRS part of the superstrate has been implemented by periodic metallic patches, and the absorptive part by the periodic square loops with lumped resistors. Wide out-of-band RCS reduction as well as gain enhancement has been achieved. For in-band RCS reduction, a metamaterial ground plane consisting of split ring resonators has been implemented, which achieves TM polarized incident wave absorption. In [12], a somewhat different technique has been implemented. In-band scattering has been achieved by a phase gradient metasurface (PGM) of varying sized square patches. For RCS reduction bandwidth enhancement as well as out-of-band absorption, typical surface of periodic square loops with lumped resistors has also been adopted on top of the PGM. For the PRS part, periodic square loops have been utilized. Wideband RCS reduction as well as broadside gain enhancement has been successfully achieved.

In all of the above works, resistive FSS has been utilized in order to achieve wideband absorption. This surface, consisting of lossy lumped resistors, does in fact introduce a small degree of attenuation to the radiated wave [12]. Besides, a large number of high frequency RF resistors are required, which are expensive, and consequently the overall cost and difficulty of fabrication process increases manifolds. To overcome the above shortcomings, an F-P antenna with a novel artificial magnetic conductor (AMC) surface etched in a chessboard like arrangement on top of its superstrate, with a PRS etched on its bottom, has been introduced in [14], and subsequently improved in [15]. Wideband monostatic RCS reduction as well as broadside peak radiation enhancement has been achieved simultaneously. The principle behind RCS reduction lies in the phase cancellation property of two different AMC cells [16], [17]. Likewise, a circularly polarized (CP) F-P antenna having microstrip slot array as an excitation source with sequentially rotated feeding mechanism has been reported in [18]. Unit-cell grids consisting of copper patches and areas of dielectric with no copper have been implemented in a chessboard like configuration as a superstrate. The antenna possesses wide 3 dB gain bandwidth and high broadside gain, along with wideband low monostatic RCS property (59%) realized by $180° \pm 37°$ reflection phase difference between adjacent unit-cell grids.

In order to illuminate the desired coverage area or engage particular targets, many applications demand antenna beam deflection in directions away from the horizon. To achieve that, antenna structure is mechanically tilted, but the approach is cumbersome. To solve this issue, the works presented in literature achieved electrical beam tilting by devising various involved techniques, such as using two bent conducting structures [19], employing high refractive index metamaterial loading [20], or excitation of two orthogonal odd resonant modes in a microstrip antenna having an asymmetric circular sector geometry [21]. A simple method to achieve antenna beam deflection is the use of phase gradient metasurfaces (PGMs), and the significance of PGMs increases even more as they can also realize antenna gain enhancement within the FP cavity configuration. In this regard, various PGMs have been investigated, whereby antenna beam tilting is realized by virtue of the dimensional tapering applied to the periodic unit-cells constituting the metasurface. The dimensional tapering realizes reflection phase gradient; a necessary condition for achieving radiated beam redirection. The works presented in [22]–[24] were based on a similar principle, where various beam tilt angles were achieved by varying either the capacitive grid (patch-type) or the inductive grid (loop-/aperture-type).

So, in view of the literature presented, it can be seen that meager work has been done on low RCS FP antennas which employ AMC technology, and all of those works focus on broadside gain enhancement. Prior to current work, the authors had presented two low RCS high gain tilted beam FP antennas, which were based on the integration of resistive FSS and phase-gradated composite PRS (PGM) [25], [26].

However, as discussed above also, concerning factors in [25], [26] are the requirement of large number of expensive RF resistors, their associated radiation losses, as well as the cost of assembly. Different from the previous works, in this work, we aim to design and integrate a phase gradient metasurface with AMC surface in an FP configuration, and the objectives are to achieve not only low monostatic RCS and gain enhancement, but also a fixed tilted beam radiation. As per the authors' best knowledge, this is the first work representing the implementation of PGM and AMC structures together, in order to achieve the aforementioned objectives. To achieve the desired objectives, three different unit-cell structures have been implemented. The superstrate consists of two integrated dielectric layers with the unit-cell grids etched onto them. The reflection phase of the unit-cells have been adjusted in such a way that the wideband phase cancellation principle can be leveraged for achieving low monostatic RCS, and, at the same time, the phase gradation property of the designed PRS aids the beam deflection process in the antenna's transmission mode. The antenna realizes 12 dB of gain with a tilt angle of $-60°$. Monostatic RCS reduction bandwidth is from 4-13 GHz (105.8%), and is almost identical for x/y polarizations of the incident wave. The cavity height is less than $\lambda/2$. Next, we present a modification in our first design (Ant-1). This new antenna (Ant-2) is based on two unit-cell structures, having small variations from the first design, and also the cavity aperture (footprint) becomes smaller. However, the RCS reduction bandwidth is slightly different for the two orthogonal polarizations of the incident wave. It is 105.8% for x-polarization (x-pol) and 85.7% for y-polarization (y-pol), respectively. The achieved gain is almost 12 dB, with tilt angle of $-37°$. The cavity height in this case is also less than $\lambda/2$. Simulation results of both designs have been presented. Ant-1 has been fabricated also for design validation. The applications of the presented work can be in side looking air-borne radars (SLARs) [27], any surveillance application requiring communication above or below the horizon, or in low scattering multiple-input multiple-output (MIMO) antennas with radiation pattern decorrelation [28].

II. PROPOSED FP ANTENNA AND DESIGN PROCEDURE

A. RCS REDUCTION PRINCIPLE

Originally, Paquay [29] proposed a chessboard like configuration, consisting of a combination of AMC and perfect electric conductor (PEC) cells, to achieve RCS reduction based on phase cancellation principle. Metallic patches constituted the PEC part, and Sievenpiper's mushroom structures constituted the AMC part. In this, RCS reduction is achieved based on destructive interference between the wave contributions reflected from PEC and AMC parts. For an incident wave, PEC cells introduce a 180° reflection phase shift, while AMC cells, at their operating frequency, reflect the wave with no phase change. These contributions with opposite phases cancel out in the specular direction for an incident wave, achieving a null, and hence RCS is lowered.

The above configuration has narrow RCS reduction bandwidth as AMC is band limited in its frequency response. To address this limitation, two appropriately designed AMC cells having different resonance frequencies are utilized that can achieve phase cancellation over a broad bandwidth [16], [30]–[32]. The reflection phase difference of $\Delta = 180 \pm 37°$ (i.e., from 143°-217°) between two AMC structures ensures RCS reduction of 10 dB or greater, and can be computed based on the empirical relation derived in [30] as:

$$\text{RCS reduction} = 10\log_{10}|[A_1\exp(\mathrm{j}P_1) + A_2\exp(\mathrm{j}P_2)]/2| \tag{1}$$

where A_1 and A_2 are the magnitudes of reflection coefficient of AMC structures, and P_1 and P_2 are the reflection coefficient phases of the two AMCs. The proposed unit-cell structures in our paper are inspired from [31], owing to their simple geometry, desired frequency resonance, and importantly, appropriate slope of reflection phase curve. The details of unit-cell configurations and their scattering (S) parameters are discussed next.

B. UNIT-CELL DESIGN

The proposed FP antenna incorporates 3 unit-cells. Two of them are typical AMCs, and are designated here as AMC-1 and AMC-2. The primary purpose of AMC-type cells is to achieve backscattering reduction. The third unit-cell is an FSS by virtue of which phase gradient is implemented to achieve antenna beam deflection. Moreover, the FSS-grad cells also play their part in conjunction with AMC-type cells to achieve backscattering reduction. The third unit-cell is designated here as FSS-grad.

Fig. 1 shows the configuration of AMC-1. Its perspective view along with port designations is shown in Fig. 1(a). It consists of a metallic square patch etched on top side of the upper dielectric (Fig. 1(b)). A full metal plane with an aperture (metallic part etched-off) in its center forms the top layer of lower dielectric (Fig. 1(c)). A metallic square patch constitutes the bottom side of lower dielectric (Fig. 1(d)). Both dielectrics are separated by an air gap (g).

Fig. 2 shows the configuration of AMC-2. The 3D view is shown in Fig. 2(a). Its upper dielectric consists of a square metallic loop with a square patch in its center (Fig. 2(b)). The design of the lower dielectric of AMC-2 (Fig. 2(c) and 2(d)) is identical to AMC-1 (Fig. 1(c) and 1(d)). The two dielectric layers are separated by an air gap.

Fig. 3 shows the configuration of third unit-cell, FSS-grad. The perspective view with port numbering is shown in Fig. 3(a). Its upper part is a bare dielectric (Fig. 3(b)), the top side of lower dielectric forms an aperture (A_V) of variable size (Fig. 3(c)), while its bottom side consists of a square metallic patch (Fig. 3(d)). The two dielectrics are separated by an air gap.

In order to form a phase gradient metasurface (PGM) using the FSS-grad cells, the variation of its aperture (A_V) size will be realized once the FSS-grad cells are implemented in a

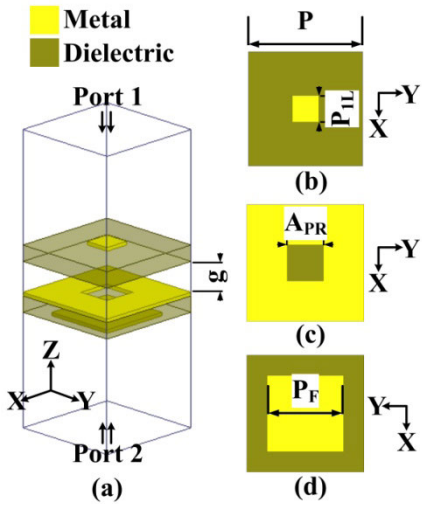

FIGURE 1. AMC-1 unit-cell design. (a) Perspective view. (b) Top side. (c) Middle. (d) Bottom side.

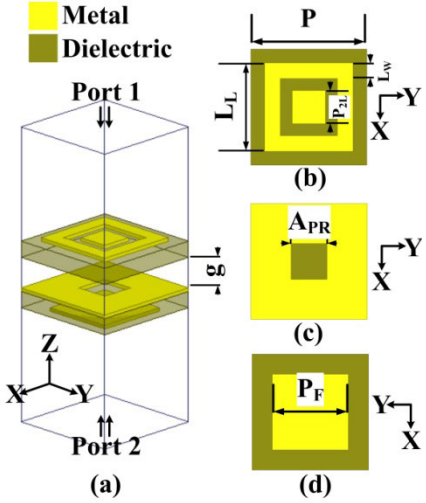

FIGURE 2. AMC-2 unit-cell design. (a) Perspective view. (b) Top side. (c) Middle. (d) Bottom side.

periodic fashion over the aperture of the FP cavity antenna. For the wave radiated from the patch antenna, the varying A_V sizes will yield the necessary reflection phases (reflection phase gradient) as well the magnitude, thereby achieving the antenna beam tilt along with a higher gain. Moreover, in order to achieve broadside monostatic RCS reduction, an appropriate combination of all the three unit-cell types will be implemented over the aperture of the FP antenna. In a nutshell, a certain periodic implementation of the three unit-cell types over the FP cavity aperture will help realizing not only high gain and tilted beam radiation, but will also aid in achieving a wideband monostatic RCS reduction in parallel. Thus, to investigate the RCS reduction phenomena together with gain enhancement and tilted beam operation, the reflection coefficient responses of the designed unit-cells are necessary to understand, and are presented next. The exact configuration of the FP cavity aperture consisting of the three unit-cell types will be discussed in sub-section C.

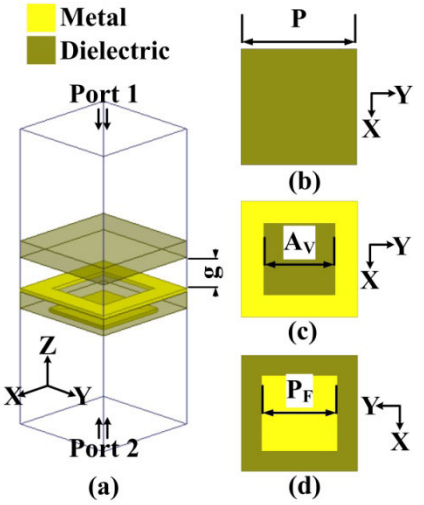

FIGURE 3. FSS-grad unit-cell design. (a) Perspective view. (b) Top side. (c) Middle. (d) Bottom side.

C. UNIT-CELL S-PARAMETERS ANALYSIS

Unit-cell simulations were performed in High Frequency Structure Simulator (HFSS), and the simulation setup incorporated periodic boundary conditions and Floquet port excitations. The three unit-cell simulation models are displayed correspondingly in Fig. 1(a), Fig. 2(a), and Fig. 3(a).

Initially, the unit-cell results that model the antenna's RCS reduction are presented. Thus, for a wave incident along $-$z-axis, the phase and magnitude responses of the reflection coefficient (S_{11}) for the three unit-cell types are shown in Fig. 4(a) and 4(b), respectively. From Fig. 4(a), it can be seen that the reflection phase condition of $\Delta = 180° \pm 37°$ between AMC-1 and AMC-2 is being met from 4.3-12.1 GHz (95.12%). Likewise, for FSS-grad and AMC-2, where the aperture (A_V) of FSS-grad is being varied from 1 mm to 7 mm, it can be witnessed that from 4.4-12 GHz (92.68%), the reflection phase difference lies within the said range ($180° \pm 37°$). The results imply that the reflection phases of FSS-grad (despite having varying A_V values) and AMC-1 are quite identical, while the reflection phase of AMC-2 is such that over a wide band, it will realize a destructive interference with the reflection phases of AMC-1 and FSS-grad. Thus, once the FP configuration is constructed having a superstrate with an appropriate arrangement of these unit-cells, it is expected that a wideband monostatic RCS reduction of about 94% or higher would be achieved. This will be elaborated further when the FP antenna configuration will be presented (sub-section C).

The magnitude response of reflection coefficients of AMC-1, AMC-2 and FSS-grad are shown in Fig. 4(b). Over the entire frequency range, it is evident that the values of reflection magnitude of AMC-1 and AMC-2 are above 0.94. The reflection magnitudes of FSS-grad are about 0.7 and above. The reflectivity values of FSS-grad increase as the aperture size (A_V) reduces. Nevertheless, the minimum magnitude is still high enough to significantly reflect the incident wave in order to achieve appropriate destructive interference with the waves reflected from AMC-2.

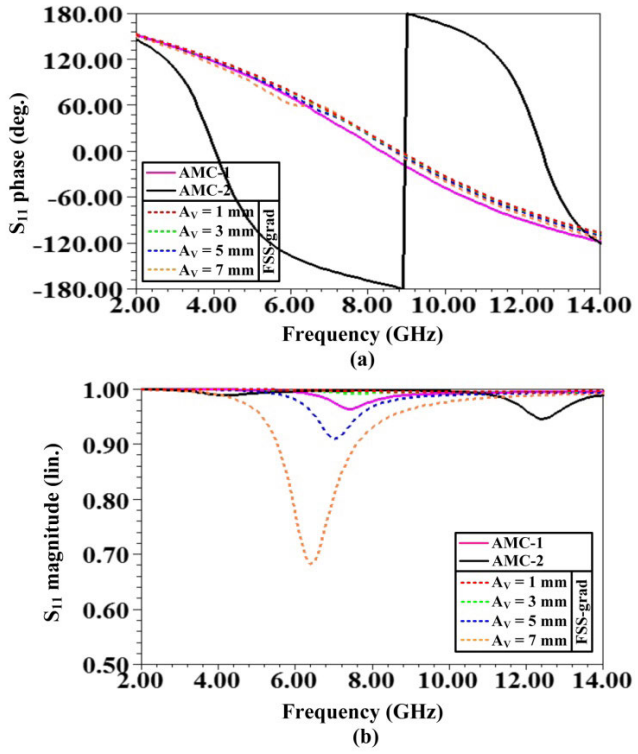

FIGURE 4. Reflection coefficient response of AMC-1, AMC-2, and FSS-grad for a wave incident along −z-axis. (a) Phase response. (b) Magnitude response.

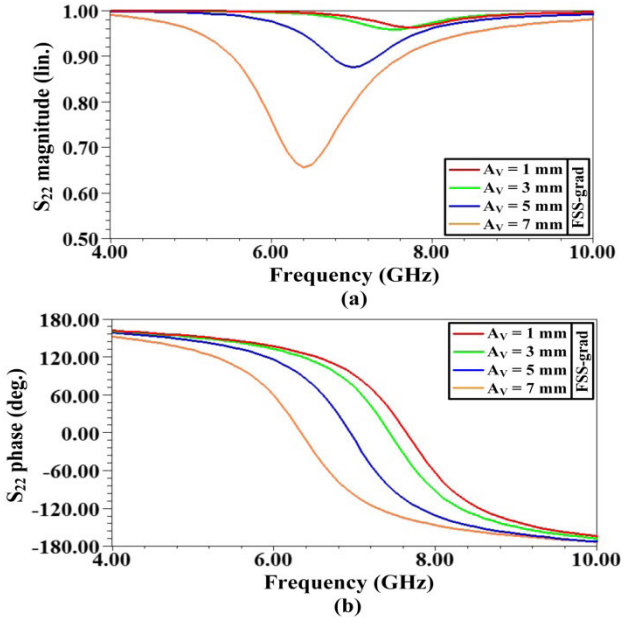

FIGURE 5. Reflection coefficient response of FSS-grad for a wave incident along +z-axis. (a) Phase response. (b) Magnitude response.

Now, the unit-cell results that model the antenna's high gain deflected beam operation are presented. For the incident wave towards +z-axis, the reflection coefficient response (S_{22}) of FSS-grad is shown in Fig. 5, for the aperture size (A_V/gradient) values ranging from 1 mm to 7 mm. The results shown in Fig. 5 are significant as these model the response of FSS-grad for a wave emanating from the patch antenna (excitation source of the FP cavity) and striking the FSS-grad cells. Magnitude response is shown in Fig. 5(a). The variation of magnitude values is in due accordance with the aperture size (A_V). At operating frequency (7 GHz), the reflection magnitude is 0.79 and above. This reflectivity is high enough to realize gain enhancement of the cavity's excitation source (patch antenna). Fig. 5(b) displays the phase response of reflection coefficient. As can be seen, at 7 GHz, a phase gradient ranging from +90° to −99° has been successfully achieved, realized through varying aperture sizes (A_V values). So, from Fig. 5, it can be concluded that high reflectivity values along with varying reflection phases (reflection phase gradient) of the FSS-grad are suitable for implementing the FSS-grad cells as gradated PRS (phase gradient metasurface) above the excitation source in an FP cavity configuration. This will aid in achieving not only the gain enhancement, but antenna beam tilting would also be realized. Moreover, the reflection phase values are about in the range ±90°; this implies that the FP cavity height can also be lowered to less than λ/2, where λ is free space wavelength at the operating frequency of the excitation source [24]. In the transmission mode of the antenna, only the reflection properties of the FSS-grad are important, as directly above the excitation source (patch antenna) at an appropriate height, the PRS consisting of FSS-grad unit-cells will be implemented in the FP configuration. Therefore, it is expected that the reflection properties of AMC-1 and AMC-2 will not render a too significant impact on the radiation characteristics of the antenna [33]. Nevertheless, for the sake of completion, the reflection magnitude and phase responses of AMC-1 and AMC-2 are presented in Fig. 6(a) and 6(b), respectively. High reflection magnitudes (above 0.95) and almost similar reflection phases can be witnessed for the two AMCs at 7 GHz.

D. FP ANTENNA MODEL

Based on the presented unit cells in the previous section, the simulated model of the proposed FP antenna is shown in Fig. 7(a), and its fabricated prototype is shown in Fig. 7(b). As can be seen, grids of unit cells have been integrated in a side by side arrangement to form the superstrate assembly, and then are placed above the patch antenna in an FP cavity configuration. The following guidelines were followed to integrate the unit cells [15], [30], [31], [33], [34]:

a) As the FSS-grad cells are primarily designed to offer reflection phase gradient for the wave radiated from the patch radiator, they should be placed directly above the patch antenna. The implemented grid size of 5 × 5 offers an adequate flexibility to achieve the radiation beam tilt, which, in fact, is based on the reflection phases of the varying A_V values.

b) In order to have identical RCS reduction performance for orthogonal polarizations of the incident wave, the interfaces of destructive interference should appear symmetrically along both axis (x and y).

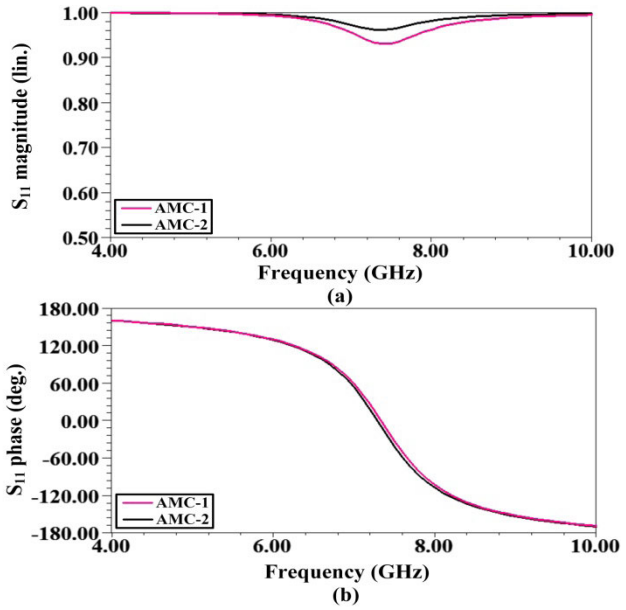

FIGURE 6. Reflection coefficient response of AMC-1 and AMC-2 for a wave incident along +z-axis. (a) Magnitude response. (b) Phase response.

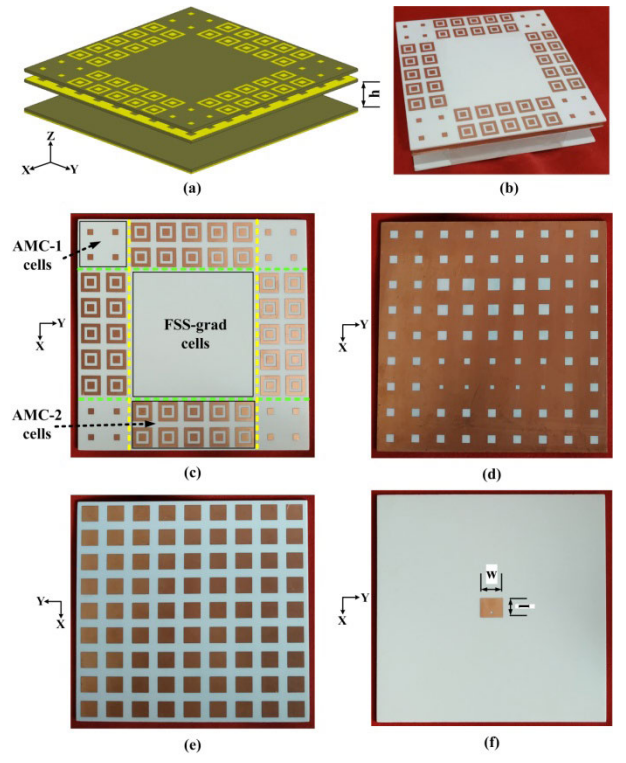

FIGURE 7. Simulated model and fabricated design. (a) HFSS simulation model. (b) Fabricated model. (c) Top dielectric. (d) Top side of lower dielectric. (e) Bottom side of lower dielectric. (f) Patch antenna as FP cavity excitation source.

The top layer exhibiting integration of the three unit-cell structures is shown in Fig. 7(c); labelling of the different unit-cell types can also be witnessed. Also shown are the interfaces of destructive interference represented by the yellow and green dashed lines, for x- and y-axis respectively. Across the interface lines, a parallel (or side by side) placement of those unit-cells can be seen that satisfy the phase cancellation property. Thus, either, FSS-grad and AMC-2 cells are seen lying across the interfaces in parallel, or, AMC-1 and AMC-2 cells are seen lying across the interfaces. Across the interfaces, there is no instance where FSS-grad and AMC-1 cells are lying in parallel; this is because they have almost identical reflection phases. Moreover, it can also be witnessed that placement of the three unit-cell types is in a symmetric fashion over the entire superstrate surface; an aspect important to achieve identical RCS performance for arbitrary polarizations of the incident wave. This will be further confirmed with the Ant-1 RCS results presented in section III-B.

The top side of lower dielectric consisting of fixed and variable apertures (gradient) is displayed in Fig. 7(d). Fig. 7(e) illustrates the bottom layer of lower dielectric; fixed patches constitute this part. Lastly, a coaxial fed rectangular patch antenna with its dimensions is shown in Fig. 7(f). Its operating frequency is 7 GHz, and has been employed as the excitation source for the FP cavity. Its feeding point is displaced 2.4 mm towards +x-axis from the patch center. All dielectric layers have been constructed from Rogers RO4003C laminate having dielectric constant of 3.38 and dielectric height of 1.52 mm. Foam type air gap spacers have been used to hold the antenna dielectrics at appropriate heights.

The cavity height (h) at resonance is based on following relation [35]:

$$h = [(\varphi_{PRS} + \varphi_G)/\pi]\lambda/4 + N\lambda/2 \tag{2}$$

where φ_G = reflection phase of ground (π), φ_{PRS} = reflection phase of PRS, λ is free space wavelength at operating frequency, and $N = 0$ (zeroth order resonance). Since the reflection phase of a phase gradated PRS is not fixed, and alters along its surface, equation (2) just serves as a guide to determine an initial cavity height. If $\varphi_{PRS} = 0$, the cavity height will be $\lambda/4$ (10.7 mm). However, considering the proposed design, φ_{PRS} varies between $\pm 90°$ at the operating frequency (evident from Fig. 5(b)). Thus, finalized resonant cavity height ($h = 14$ mm) has been obtained through simulations.

The final dimensions of the unit-cells as well as FP antenna are shown in Table 1. Likewise, the final PRS gradient values with corresponding reflection magnitudes and phases are shown in Table 2. Gradient has been implemented along x-axis, which is the E-plane of the antenna.

In order to reach to the finalized gradient values, it is well known that a dimensional gradation (non-uniformity) introduced to the PRS elements results in a progressive phase shift, and thus the radiation beam deflection towards elements depicting a phase lag [36]. In this context, it was noted from [23], [24], [28] that a constant dimensional gradation in the PRS elements had been implemented in order to achieve a beam tilt. The constant dimensional gradation here means that the difference of size between two consecutive unit-cell elements was fixed. However, in our proposed design, though the implementation of a constant dimensional gradation in the

TABLE 1. Dimensions of unit-cells and FP antenna.

Dimension	Value (mm)	Dimension	Value (mm)
P	13	L_W	1.75
P_{1L}	4	P_{2L}	3.7
A_{PR}	4	A_V	variable
P_F	8.5	h	14
g	4	l	9.9
L_L	9.9	w	11.6

TABLE 2. Finalized gradient values of Ant-1.

A_v	Phase	Magnitude
2	89.83°	0.98
3	71.48°	0.97
4.7	7.87°	0.90
5.4	-32.91°	0.84
6.2	-75.63°	0.81

PRS elements did result in the tilted beam formation, some higher side lobes were also witnessed. Therefore, to reduce the side lobe levels along with achieving a good tilt angle, parametric optimization was also leveraged. Some simple parametric tuning of each A_V value was performed through simulations, which resulted in the finalized gradient values (A_V) as listed in Table 2. In this work, we just ensured to obtain a noticeable beam deflection to validate the design concept, irrespective of how much is the extent of tilt. It should be noted that a different set of PRS gradient values would be required in order to direct the beam to a different tilt angle. In this regard, a theoretical model presented in [33] might stand as a useful tool in anticipating the tilt angles; however, further characterization of the side lobes might still be required.

As is evident from Fig. 7 (top side), FSS-grad unit-cells form the central 5 × 5 part of the superstrate grid. AMC-1 and AMC-2 unit-cells surround the FSS-grad cells as shown in the figure. To achieve RCS reduction based on phase cancellation principle, only two different AMC unit-cells are required. In fact, it is two different reflection phase responses that should meet the phase cancellation criteria to reduce the RCS. In our proposed design, an additional unit-cell (FSS-grad) has also been introduced. This additional unit-cell has been designed in such a way that its reflection coefficient's (S_{11}) phase response matches the phase response of one of the AMCs; in our case, AMC-1. That is the reason it has been incorporated/integrated on top side of the superstrate, with AMC-1 and AMC-2, to achieve appropriate wideband RCS reduction. Also, its S_{22} phase response shows a progressive phase change with varying aperture sizes (A_V values). This means that it can offer the desired reflection phase response to achieve radiation beam tilting. This forms the basis to place it at the center of the superstrate, directly above the patch antenna. Therefore, the FSS-grad is the key of the proposed

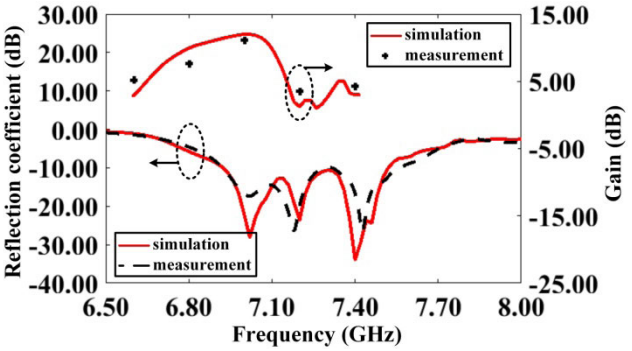

FIGURE 8. Reflection coefficient plot and gain vs. frequency curve of the proposed antenna.

design, which has been leveraged along with AMC-1 and AMC-2 in the FP configuration, to achieve in parallel, the monostatic RCS reduction, high gain, and off-broadside radiation. The area of the superstrate occupied by unit-cells of FSS-grad together with AMC-1 is almost equal to the area occupied by AMC-2 cells, as visible by the arrangement shown in Fig. 7 (top side). Besides, the arrangement is symmetric. For RCS reduction, such arrangement ensures symmetric RCS reduction for orthogonal polarizations of the incident wave.

Further elaboration regarding the adopted configuration of the cavity aperture of Ant-1 is presented in detail in section VII.

III. SIMULATION AND MEASUREMENT RESULTS

The unit-cell results discussed in the previous section were based on periodic boundary setup in HFSS. The simulation setup consisting of periodic boundaries considers the structure (unit-cell) to be repeated infinitely. In the FP antenna configuration (as in Fig. 7(a)), a finite number of unit cells are laid to constitute the structure, and to determine the accurate response of the full structure, the HFSS simulations were performed using radiation boundary setup. This simulation setup does undertake the truncation effect, meaning the finiteness of the structure is considered while solving for the solution. Therefore, the obtained results discussed in this section are in fact the response of the actual finite structure, and have further been validated by measuring the fabricated prototype. For performing far-field measurements, fabricated prototype was tested in the anechoic chamber. Besides, the antenna's S_{11} was measured on a vector network analyzer. Detailed radiation and RCS results are presented next.

A. FP ANTENNA RESULTS

Fig. 8 illustrates the reflection response S_{11} of the designed FP antenna. Measured result is also included. It can be seen that the antenna is matched over a wide impedance bandwidth (BW), from 6.92-7.52 GHz. At 7 GHz, which is the design frequency of the FP cavity, the value of S_{11} is below −22 dB, which shows that antenna is well matched at the operating frequency. The impedance bandwidth (−10 dB) is

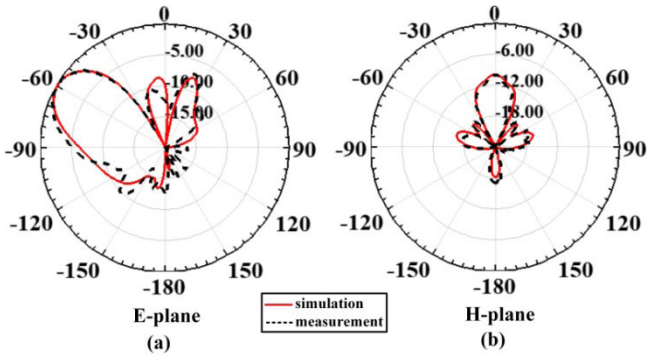

FIGURE 9. Radiation pattern plots of the designed FP antenna. (a) E-plane (x-o-z plane). (b) H-plane (y-o-z plane).

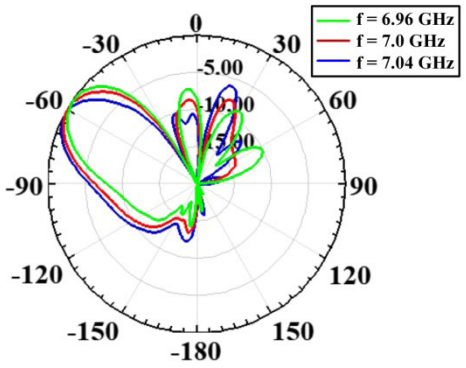

FIGURE 10. E-plane (x-o-z plane) radiation plot at different frequencies.

600 MHz (8.3%). It can also be witnessed from the figure that the measured S_{11} plot is in good agreement with the simulated result.

The gain vs. frequency plots of the FP antenna is also shown in Fig. 8. It can be seen that peak gain of 12 dB has been achieved at 7 GHz. 3 dB gain bandwidth extends form 6.75-7.11 GHz. This equals 360 MHz (5.19%). It should be remembered that FP antennas have inherently narrow radiation bandwidth, due to high Q-factor of the FP resonators [37]. The measured plot is in accordance with the simulated result.

Next, E-plane and H-plane radiation patterns of the proposed FP antenna at operating frequency (7 GHz) are shown in Fig. 9. As the gradient implementation is along x-axis, which is the E-plane of the antenna, therefore, beam tilt can be witnessed in the E-plane pattern, as shown in Fig. 9(a). The main lobe has been deflected towards an off-broadside direction, and quite good beam tilt has been achieved. The peak value is appearing at an angle of $-60°$. The side lobe levels (SLLs) are about -8 dB and below. The angular direction of tilt and the increase of gradient aperture size are in the same axis, i.e., $-$x-axis. Similarly, Fig. 9(b) displays the H-plane pattern. Measured results for Fig. 9(a) and 9(b) agree well with the simulated results. For E-plane pattern, the half power beamwidth (HPBW) is 35°, and for H-plane pattern, HPBW is 41°.

To investigate the pattern bandwidth of the proposed design, radiation pattern is plotted over various frequencies

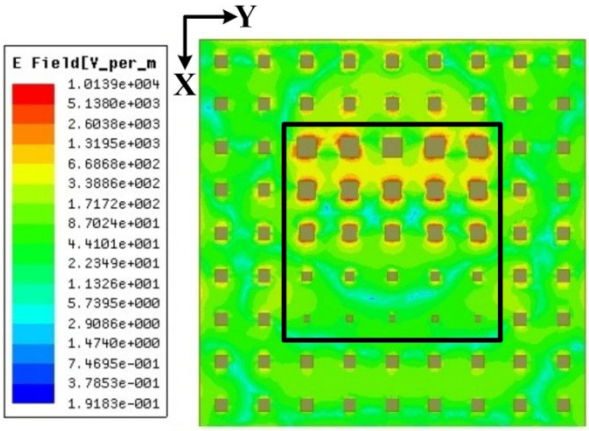

FIGURE 11. E-field overlay plot on the surface holding gradated apertures (gradient layer).

and the results are shown in Fig. 10. From 6.96-7.04 GHz, the beam pattern is quite uniform with almost identical beam deflection; however, the side lobes deteriorate to some extent. The pattern bandwidth turns out to be ∼80 MHz.

To have further understanding of the beam tilt phenomena at operating frequency, E-field overlay plot on the surface that holds the gradated apertures (gradient layer) is displayed in Fig. 11. The gradient part is shown enclosed within a square boundary. It can be observed that an increase of E-field intensity occurs with increasing aperture sizes (A_V values). The incremental field is along $-$x-axis, thereby realizing main beam deflection towards the same direction in the elevation plane. Slight increase of field intensity in nearby fix-sized apertures is because of the phenomena of field coupling among the apertures.

B. RCS RESULTS

In this sub-section, monostatic RCS performance of the proposed FP antenna in terms of frequency and angular response will be presented. Fig. 12(a) illustrates the simulated monostatic RCS frequency response of the FP antenna/reference antenna/flat plate of identical dimensions, for a normal-incident plane wave with vertical polarization (VP). VP corresponds to x-axis of the simulated model. The designed FP antenna without the superstrate structure is referred to as the reference antenna in the manuscript. It is basically a patch antenna having a ground plane of lateral dimensions identical to those of the designed Fabry-Perot cavity. The flat plate RCS has been calculated using the following equation:

$$\sigma_{FP} = 4\pi(L \times W)^2/\lambda^2 \tag{3}$$

where, σ_{FP} is the radar cross section (in m^2) of a flat metal plate, $L \times W$ is the area of the flat plate with L representing its length and W width, and λ is the wavelength over which RCS is being considered.

In Fig. 12, as can be seen, RCS reduction has been achieved over a broad bandwidth, and includes the in-band frequencies also. The reduction has been achieved from 4 GHz to 13 GHz, which amounts to a remarkable 105.88% BW. This fully

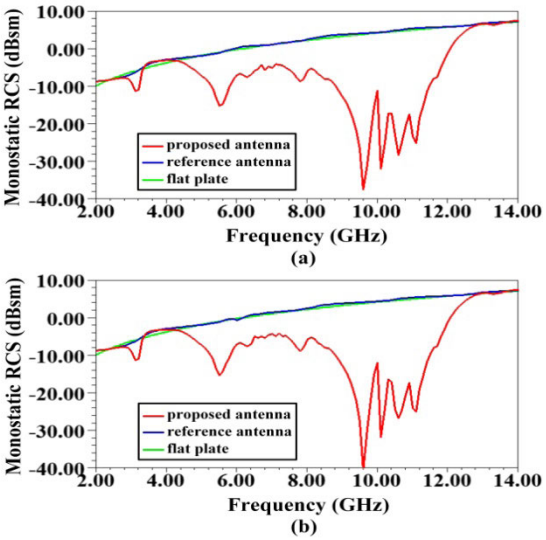

FIGURE 12. RCS frequency performance for a wave with normal incidence. (a) VP. (b) HP.

includes the C and X band where majority of radars are deployed. Fig. 12(b) illustrates the simulated RCS frequency response for horizontally polarized (HP) incident wave, and an almost similar response can be witnessed when compared to Fig. 12(a). This owes to the symmetric design of unit-cells, as well as their symmetric implementation in a periodic configuration over the superstrate. For both plots, the maximum value of RCS reduction is above 40 dB achieved at 8.6 GHz. The average RCS reduction from 4-13 GHz is 12.18 dB for the case of VP incident wave, and it is 12.25 dB for HP incident wave. For most of the frequencies, the value of RCS reduction is 10 dB or higher, except around 7 GHz, which is the FP antenna's operating frequency band. The RCS reduction is slightly lower in the operating frequency band; this might be because of the difference between the values of reflection (S_{11}) magnitude of FSS-grad unit-cell and AMC-2 unit-cell. For FSS-grad, it is about 0.8 and above around operating frequency, while for AMC-2, its value is above 0.94 over the entire band. This difference of amplitude may be the cause of some diminished remnant reflected wave even after the phase cancellation of reflected waves from the two unit-cell surfaces has occurred. Nevertheless, the in-band RCS reduction value for VP is 6.18 dB and above, and for HP it is 5.7 dB and above.

To confirm the RCS reduction, measured samples (FP antenna/reference patch antenna) were tested while having a 50 Ω termination. Transmit (Tx) and receive (Rx) parabolic reflector antennas excited by λ/2 long wire dipole sources were employed. Two such sets were locally fabricated within the lab facility, and measurement was performed on six distinct frequencies. A notable advantage achieved with this setting is because of the small size of these antennas; whereby, the ideal monostatic conditions in simulation are more closely followed in a real measurement setup. This owes to the shorter center to center distance between Tx and Rx antennas. The monostatic RCS reduction performance for VP and HP wave

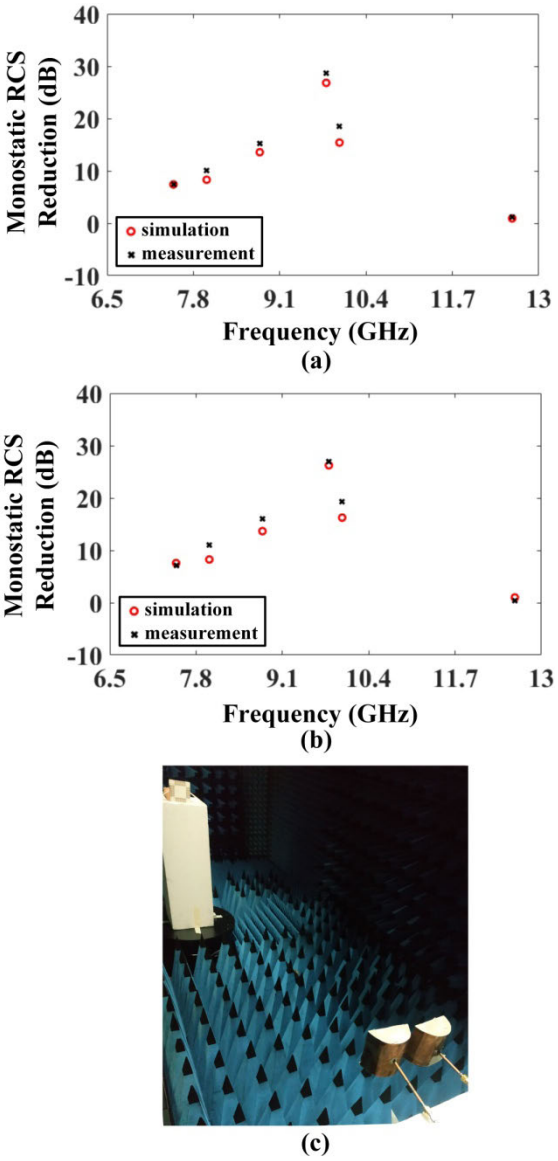

FIGURE 13. RCS reduction plotted at distinct frequencies for orthogonally impinging wave. (a) VP wave. (b) HP wave.

incidences are shown respectively in Fig. 13(a) and 13(b). The measurement setup is also displayed in Fig. 13(c). A remarkable agreement can be observed between simulated and measured values on every frequency, establishing the proof of concept validity of the designed prototype. Table 3 details the RCS reduction performance achieved for VP and HP wave incidences at the measured frequencies. For both wave incidences, the averaged-out difference between simulated and measured RCS reductions is lower than 1.5 dB.

The monostatic RCS performance has also been investigated against oblique incident angles (+90, −90) of the wave in order to see the angular stability of the proposed design. The results are presented for x-o-z plane and y-o-z plane, with horizontal and vertical wave polarizations, respectively. The corresponding RCS results of the reference antenna are also shown along with. For normalized y-o-z plane, the

TABLE 3. RCS reduction performance at measured frequencies.

Ser.	Freq.[a] (GHz)	RCS Reduction (dB)			
		Sim.[b] (VP)	Meas.[c] (VP)	Sim. (HP)	Meas. (HP)
1.	7.5	7.41	7.44	7.56	7.17
2.	8	8.31	10.13	8.25	11.05
3.	8.8	13.57	15.29	13.66	16.02
4.	9.8	26.81	28.65	26.23	26.95
5.	10	15.41	18.56	16.24	19.27
6.	12.6	0.93	1.15	0.99	0.35
Average Reduction (dB)		12.07	13.54	12.16	13.47

[a]Freq.: Frequency, [b]Sim.: Simulation, [c]Meas.: Measurement.

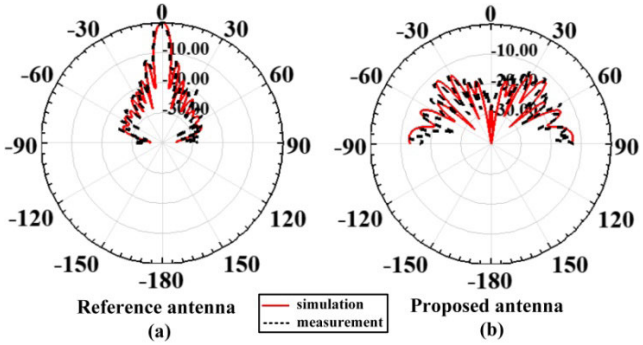

FIGURE 14. Normalized RCS performance for oblique angle wave incidences in y-o-z plane with VP impinging wave. (a) Reference antenna. (b) Proposed antenna.

simulated and measured monostatic RCS plots for VP wave are shown in Fig. 14(a) for reference antenna, and Fig. 14(b) for the proposed antenna. These results have been plotted at 9.8 GHz. The results show that RCS reduction is occurring over the angular range of ±13°, with maximum RCS reduction approaching ∼27dB. Similarly, normalized x-o-z plane RCS performance for HP incident wave is displayed in Fig. 15(a) for the reference antenna, and Fig. 15(b) for the proposed antenna. Here also, the angular stability of ±13° has been attained with maximum RCS reduction value of ∼27 dB. The narrow beam-width of the reflectivity pattern of the reference patch antenna shown in Fig. 14(a) and Fig. 15(a) is because of its relatively larger ground plane, which, as previously mentioned, is same size as of the lateral dimensions of the FP cavity. The measured results show considerable agreement with the simulation plots. All scattering results (frequency/angular) have been presented for the case where antennas were terminated in a matched impedance.

To analyze the mechanism of RCS reduction, E-field distribution on top surface of the superstrate of the FP antenna is shown in Fig. 16 (a), plotted at 9 GHz for VP incident wave. Different field distributions can be witnessed from the plot. High concentration of E-field occurs over AMC-2 unit-cells, whereas almost identical field distribution can be observed over AMC-1 unit-cells and FSS-grad surface. The different field resonance states over the surface of the superstrate provide the necessary reflection phase difference

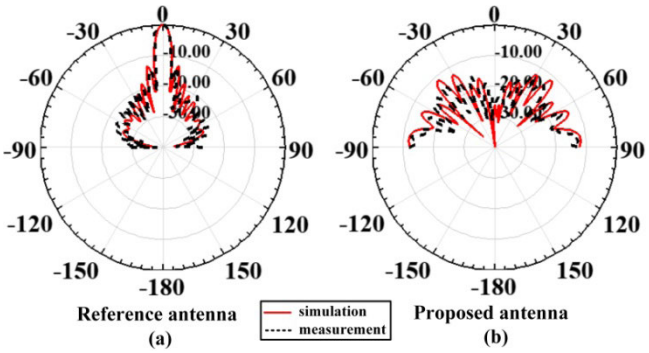

FIGURE 15. Normalized RCS performance for oblique angle wave incidences in x-o-z plane with HP impinging wave. (a) Reference antenna. (b) Proposed antenna.

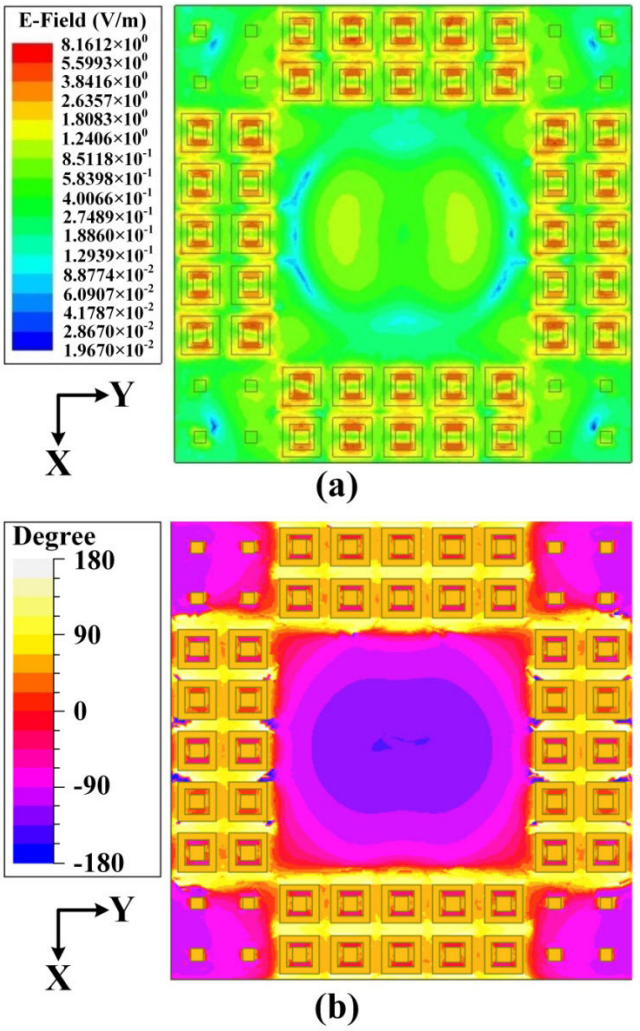

FIGURE 16. Field overlay plots on top surface of the FP cavity for VP incident wave at 9 GHz. (a) E-field's magnitude distribution. (b) E-field's phase distribution.

that is leveraged to achieve backscattering reduction. This is further validated by the E-field phase distribution plot shown in Fig. 16(b). By inspecting the figure, it can be readily verified that the reflection phases on the FSS-grad surface

are almost identical to the reflection phases on AMC-1 unit-cells, whereas the reflection phases on AMC-2 unit-cells are different. Furthermore, the two different phase regions have nearly opposite reflection phases, thus fulfilling the phase cancellation condition for RCS reduction. As the unit-cells are symmetrically located over the surface of the superstrate, an identical field resonance behavior is supposed for HP incident wave also.

Before concluding this section, it is also important to briefly highlight how the presented design of Ant-1 would be modified in case it is desired to have a low RCS design with broadside radiation. To this end, it is well known that the implementation of a PRS having constant unit-cell dimensions (i.e., no gradation) leads to the emanation of a radiation beam that is directed towards broadside [35]. Thus, in the proposed design, it can be achieved by removing gradation in the unit-cell dimensions of FSS-grad. This entails determining an appropriate constant A_V value for the design. Besides, to achieve a proper radiation beam with diminished side lobes, it is also important to consider parameter P_F while determining a proper A_V value. These two parameters primarily control the cavity's reflectivity for the wave radiated from the patch antenna [15]. Moreover, to achieve cavity resonance, i.e. high gain, the height of the cavity (h) should also be re-considered in parallel with the parameters A_V and P_F. Finally, for achieving input impedance matching, the location of coaxial feed point as well as the patch antenna's width may also require some further fine tuning. As regards to the RCS performance of the broadside design, it is expected to remain almost similar to as it is for the tilted beam design. This is because the parameters which require changes for the broadside design (A_V and P_F) are primarily associated with the radiation property of the antenna. However, maximum allowable variation of A_V and P_F should be determined from unit-cell simulations in order to pre-ensure there will be no adverse effect on radar waves' reflection phase characteristics.

IV. MODIFIED DESIGN (Ant-2)

Next, modification of the first design is presented. The main motivation behind the design of Ant-2 is to simplify the design of Ant-1, in that, to use only AMC-2 with the FSS-grad. The FSS-grad cells not only realize the reflection phase gradient along with high reflectivity (condition necessary for high gain and radiation beam deflection), but also realize the opposing reflection phase with the AMC-2 cells (condition necessary for RCS reduction). Moreover, in case the condition of symmetric unit-cell placement is ignored in one principal axis (unlike Ant-1), it is highly likely that the implementation of the two unit-cell types may equally well offer the advantage of realizing a relatively smaller aperture size of the cavity. The design differences from Ant-1 consist of the following:

a) Instead of using two AMC unit-cells + FSS-grad unit-cell as in the previous design to achieve RCS reduction, here only AMC-2 + FSS-grad have been employed. The configuration and dimensions of AMC-2 have been slightly changed, while FSS-grad is exactly the same as used previously. The modified AMC-2 unit-cell will be referred to as AMC-2′.

b) The periodic arrangement of unit-cells on the superstrate of the FP cavity ignores the interface of destructive interference in one of the principal axes (y-axis), and thus realizes a smaller aperture size.

The details of the modified design are presented next. For Ant-2, only simulation results are presented.

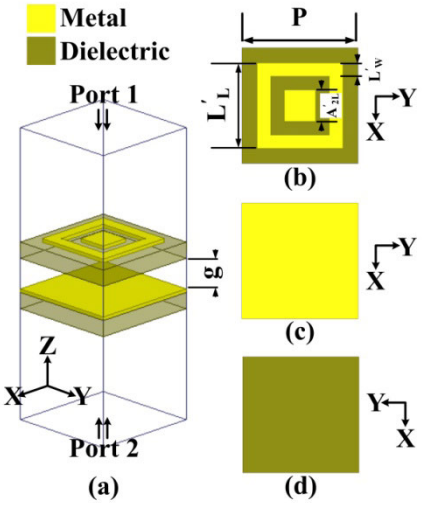

FIGURE 17. AMC-2′ unit-cell structure. (a) Perspective view. (b) Top side. (c) Full metal plane. (d) Bare dielectric bottom side.

A. MODIFIED UNIT-CELL (AMC-2′)

The configuration of AMC-2′ is shown in Fig. 17. It also consists of two dielectrics. The upper dielectric and the etched pattern on its top is similar to AMC-2 of Ant-1, only the geometric dimensions have been redesigned (shown in Fig. 17(b)). The lower dielectric has been modified, whereby now only a full metal plane is there, etched on top side of the lower dielectric (Fig. 17(c)). The bottom side of lower dielectric is bare (Fig. 17(d)). Both dielectrics are separated by an air gap. Fig. 18(a) shows its reflection coefficient's (S_{11}) phase response. Also included in Fig. 18(a) is the reflection phase response of FSS-grad of Ant-1, which has been repeated here from first design. As can be seen from the figure, the phase difference as per $\Delta = 180 \pm 37°$ between AMC-2′ and FSS-grad exists from 4.7-12.3 GHz (89.41%), and it is expected that a wideband RCS reduction would be achieved once the FP antenna configuration is constructed. Fig. 18(b) illustrates the reflection (S_{11}) magnitude response of AMC-2′, which is above 0.96 over the entire band. The reflection (S_{11}) magnitude response of FSS-grad has again been included in this figure.

B. MODIFIED FP ANTENNA MODEL (Ant-2)

The FP cavity antenna having the superstrate constructed from AMC-2′ and FSS-grad is shown in Fig. 19, which

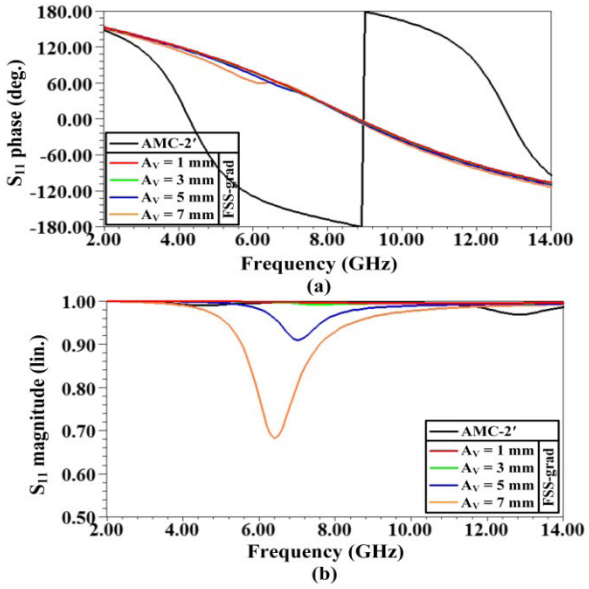

FIGURE 18. Reflection coefficient response of AMC-2′ and FSS-grad for a wave incident along −z-axis. (a) Phase response. (b) Magnitude response.

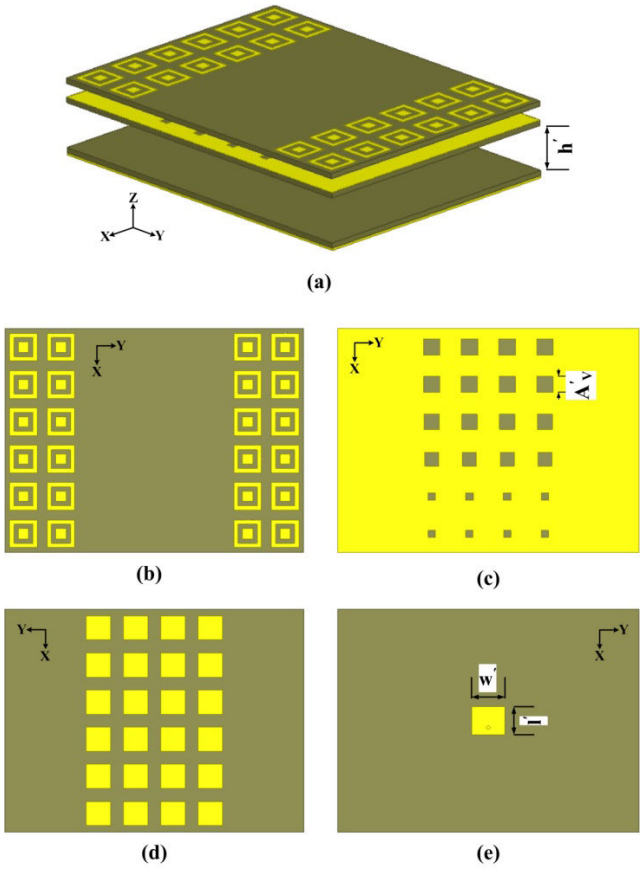

FIGURE 19. Simulated model of Ant-2. (a) Perspective view. (b) Top surface. (c) Top side of lower dielectric exhibiting gradient implementation. (d) Bottom side of lower dielectric exhibiting fixed size patches. (e) Microstrip patch as cavity excitation source.

illustrates the details of its different layers also. The designed aperture is smaller than Ant-1, and consists of a 6 × 8

TABLE 4. Final dimensions of AMC-2′ and Ant-2.

Dimension	Value (mm)	Dimension	Value (mm)
P	13	A'_V	variable
L'_L	9.6	l′	9.8
L'_W	1.5	w′	11.4
A'_{2L}	3.5		
g	4		
h′	13		

TABLE 5. Final gradient values (Ant-2).

A'_v	Phase	Magnitude
2.5	84.44°	0.98
2.6	80.11°	0.98
4.8	3.73°	0.89
5.3	-29.62°	0.85
5.6	-48.53°	0.83
5.7	-59.72°	0.83

configuration of the unit-cells. The central 6 × 4 part of the superstrate consists of the gradated unit-cells of FSS-grad, while the remaining 6 × 2 parts on the two opposite edges of the superstrate have been constructed from AMC-2′ unit-cells. The cavity is excited by a rectangular patch antenna designed at 7 GHz. The feed offset is 2.4 mm towards +x-axis from the center of the patch. Final dimensions of AMC-2′ and Ant-2 are given in Table 4. Finalized gradient values (A'_V) of Ant-2 along with their magnitudes and phases are shown in Table 5. The final A'_V values were based on a similar procedure as detailed for Ant-1 in section II-C. Moreover, as can be seen from Fig. 19(c), the central region of the dielectric consists of variable-sized apertures (A'_V), while the sides of the dielectric are formed by PEC. It should be noted that a single excitation source of the FP cavity mainly illuminates the region of the PRS that lies directly above it [38]. Thus, in the proposed design, the patch antenna mainly illuminates the central (6 × 4) region of the dielectric constituted by the variable-sized apertures (A'_V), and hence the radiation would not be blocked by the design of Fig. 19(c).

Further explanation pertaining to the adopted configuration of the cavity aperture of Ant-2 is continued in detail in section VI.

V. SIMULATION RESULTS OF Ant-2

Firstly radiation results of Ant-2 will be presented, followed by its RCS results.

A. FP Ant-2 RADIATION RESULTS

The S_{11} response of Ant-2 is shown in Fig. 20. Sharp resonance occurs at 7 GHz, with reflection coefficient value reaching −30 dB. Impedance bandwidth (−10 dB) is 160 MHz and extends from 6.92-7.08 GHz (2.3%). Gain vs. frequency curve of Ant-2 is also illustrated in Fig. 20. The

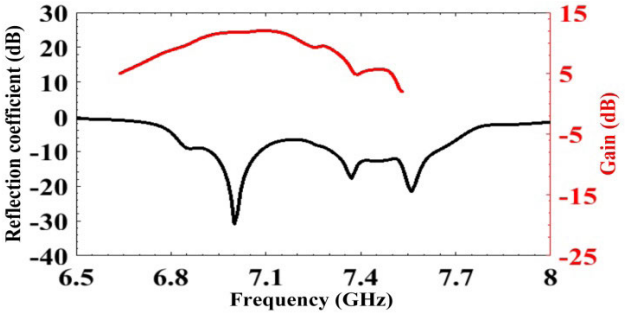

FIGURE 20. Reflection coefficient plot and gain vs. frequency curve of Ant-2.

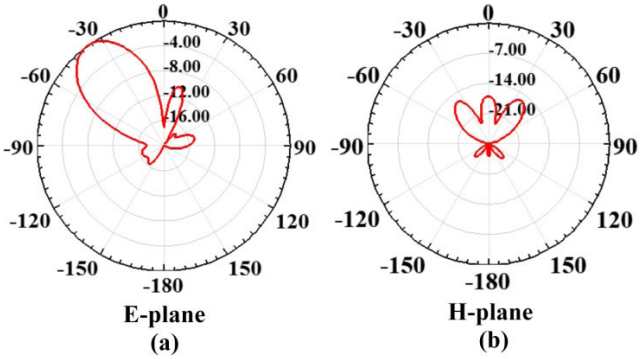

FIGURE 21. Radiation pattern plots of Ant-2. (a) E-plane (x-o-z plane). (b) H-plane (y-o-z plane).

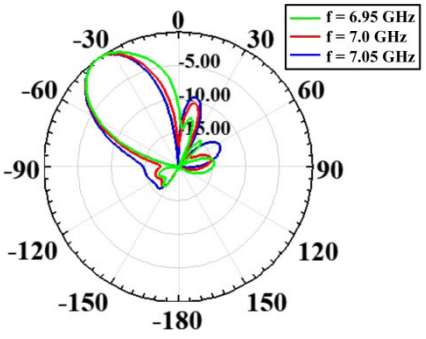

FIGURE 22. E-plane (x-o-z plane) radiation pattern plotted at various frequency points.

achieved value of gain at 7 GHz is 11.73 dB. The 3 dB gain bandwidth is from 6.8-7.31 GHz (7.23%).

The radiation patterns for the principal planes are shown in Fig. 21. E-plane radiation plot is shown in Fig. 21(a). As the implementation of gradient for Ant-2 is along the x-axis, which is also the E-plane of the antenna; therefore, the beam is deflected in the E-plane. Beam tilt angle of $-37°$ has been achieved. The SLLs are below -10 dB. The HPBW is 31°. The H-plane pattern can be seen in Fig. 21(b). Its HPBW is 18°. The radiation pattern plotted against various frequencies is given in Fig. 22. The pattern bandwidth is about 100 MHz (6.95-7.05 GHz). Slight deterioration of the side lobe performance can be seen against varying frequency; the peak radiation is maintained at $-37°$.

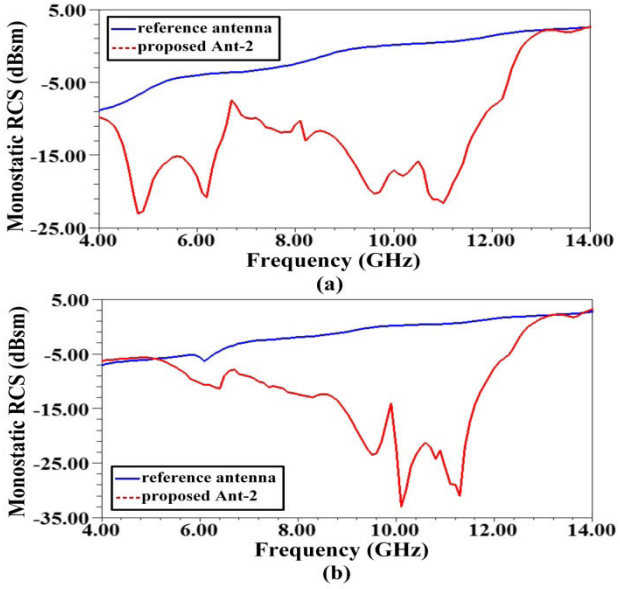

FIGURE 23. RCS frequency response of Ant-2 for a wave with normal incidence. (a) VP. (b) HP.

B. Ant-2 RADAR SCATTERING RESULTS

RCS performance of Ant-2 against frequency for VP and HP incident waves is shown in Fig. 23(a) and 23(b), respectively. Also included are the RCS frequency responses of the reference patch antenna. For VP case, wideband RCS reduction from 4-13 GHz has been achieved, which amounts to 105.8% BW. The average RCS reduction over this bandwidth is 11.56 dB. Similarly, in the HP case, RCS reduction bandwidth extends from 5.2-13 GHz. This turns out to be 85.7% BW, with average RCS reduction of 12.36 dB. The RCS plots shown in Fig. 23 are not identical for the orthogonal polarizations, although the unit-cells have been designed to be symmetric. Also the RCS reduction bandwidths are different for the two polarizations. The reason behind this lies in the macroscopic layout of the unit-cells on top of the superstrate. The layout is asymmetrical with respect to the impinging wave with different polarizations. For vertically polarized incident wave, clear interfaces of destructive interference exist along the x-axis, between the AMC-2′ cells and FSS-grad cells. However, such definite interface is not found when the incident wave becomes horizontally polarized [34]. Nevertheless, the RCS reduction BW is still greater than 85% for HP wave, and covers the in-band frequencies also.

Next, the reflection performance of Ant-2 for oblique angle (+90, −90) incident plane wave with arbitrary polarizations is presented. Fig. 24 illustrates the angular performance in x-o-z plane with orthogonal polarizations, while Fig. 25 depicts the angular response in y-o-z plane for the orthogonal polarizations. All results have been plotted at 9.6 GHz. For both figures, the corresponding plots of reference antenna are also included. In the x-o-z plane, the monostatic RCS reduction over the reference antenna has been obtained in an angular range of $\pm 10°$ for both polarizations (VP: Fig. 24(a), and HP: Fig. 24(b)). However, except a

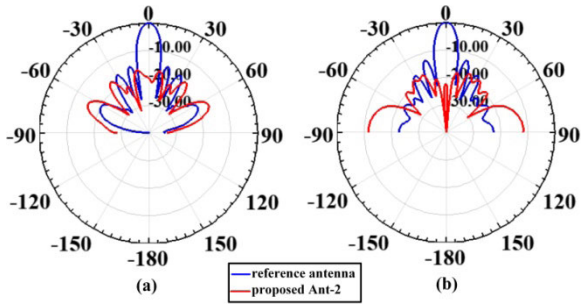

FIGURE 24. RCS for oblique angle wave incidences in x-o-z plane for Ant-2. (a) VP. (b) HP.

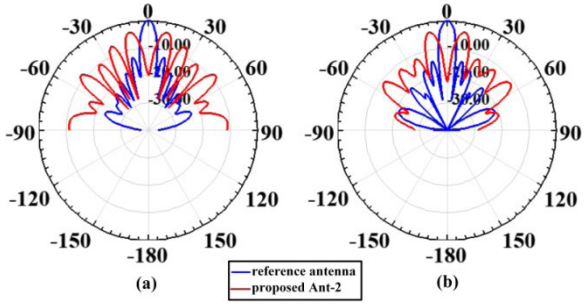

FIGURE 25. RCS for oblique angle wave incidences in y-o-z plane for Ant-2. (a) VP. (b) HP.

couple of values around ±10°, this range extends up to ±21°. Similarly, in y-o-z plane, the obtained reduction lies in the range of ±6° for both polarizations (VP: Fig. 25(a), and HP: Fig. 25(b)). In both planes, the specular reflection for normally incident waves has been reduced by at least ∼20 dB. It is to note that the RCS plots shown in Fig. 24 and Fig. 25 depict absolute RCS values in dBsm (not normalized).

Finally, for Ant-2, in order to realize a low RCS design with broadside radiation, the guidelines will be similar to as discussed for the broadside design of Ant-1 at the end of section III-B.

VI. CONSIDERATIONS OF CAVITY APERTURE SIZE OF Ant-1 AND Ant-2

In this section, the discussion regarding the cavity aperture size of Ant-1 as well as Ant-2 is presented. As regards to Ant-1 with its aperture shown in Fig. 7(c), it can be readily sized to a larger aperture size. This can be accomplished by just extending the AMC-1 and AMC-2 unit-cells to a 5 × 5 configuration, as the central FSS-grad cells are also in a 5 × 5 configuration. The scenario is shown in Fig. 26(a). If the central FSS-grad cells are increased to an n × n configuration, the AMC-1 as well as AMC-2 cells should also be increased to an n × n configuration, and vice versa [15], [17]. This will make the entire cavity aperture to be of 3 × 3 super-cell grid, and the size of the grid made of super-cells can be increased further (4 × 4, 5 × 5, etc) if desired. Fig. 26(b) shows the 4 × 4 super-cell configuration. We have chosen the central FSS-grad to be of 5 × 5 configuration, because five A_Y values offer just an adequate flexibility to realize required phase gradation for achieving tilted beam radiation.

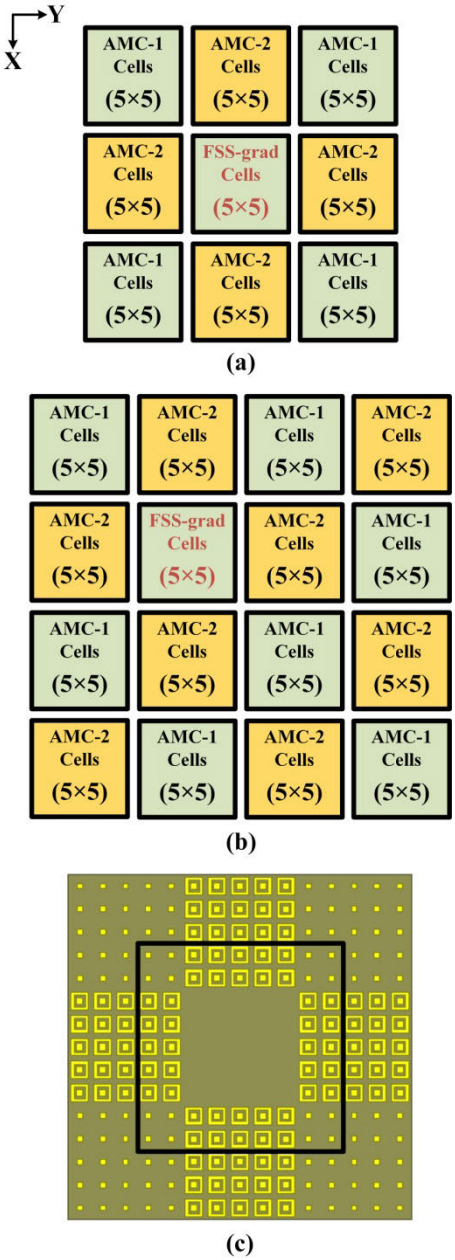

FIGURE 26. Example scenarios of cavity aperture size of Ant-1. (a) 3 × 3 super-cell grid. (b) 4 × 4 super-cell grid. (c) Square boundary indicating the adopted configuration of Fig. 7(c).

Our proposed Ant-1 shown in Fig. 7(c) is a truncated version of 3 × 3 super-cell grid of Fig. 26(a). To further clarify how the design of Ant-1 (Fig. 7) has been realized, Fig. 26(c) is represented. Fig. 26(c) follows from the implementations as reported for AMC based low RCS antenna designs in [15], [17], [18]. As clearly evident from the figure, central part shown enclosed within the square boundary constitutes the design of Fig. 7. The prime reason of adopting such a configuration was to save on the dielectric real estate, while ensuring not to compromise on the required radiation/scattering performance. Considering the arrangement of the cells, the adopted configuration shows to have nearly equal number of cells

that individually realize 0 degree and 180 degree reflection phases. FSS-grad and AMC-1 cells have almost identical reflection phases, while the AMC-2 cells have opposing reflection phase (evident form Fig. 4(a)). The surface area occupied by FSS-grad + AMC-1 cells is almost equal to the surface area occupied by AMC-2 cells. This is important because the reflected wave after striking the surface would be maximally nullified (after undergoing a proper destructive interference). The reflected wave will constitute almost equal portion of opposite reflection phases, and thus will undergo a proper cancellation.

Considering the larger configuration such as 3 × 3 super-cell grid of Fig. 26(a), the grey and brown cells have opposite reflection phases. Over this surface, the difference between the surface areas of gray and brown cells is ∼11% of the total surface area of the cavity's aperture. Nonetheless, the RCS reduction can still be appropriately achieved with such an arrangement, as supported by the results presented in [15], [17], [18]. For a 5 × 5 super-cell configuration (not illustrated here), the difference between the surface areas of opposite reflection phase unit-cells reduces further to 4% of the total area, which is even smaller than a 3 × 3 super-cell configuration. For the 4 × 4 super-cell configuration of Fig. 26(b), the surface areas of opposing reflection phase unit-cells is exactly equal. Thus, to conclude, the devised configuration of Ant-1's aperture occupies minimal dielectric space; moreover, it also ensures a proper cancellation of reflected wave components as the difference of areas between opposing reflection phase unit-cells is just ∼1%.

The placement of cells in Fig. 26(c), and thus Fig. 7(c), is symmetric along x- and y-axes. Such a placement of unit-cells offers distinct interfaces of destructive interference along both axes, and ensures identical RCS reduction for orthogonal polarizations of the incident wave [31].

Regarding Ant-2, its main purpose is to achieve RCS reduction based on only two unit-cell types, and hence a design simplification over Ant-1. This is because FSS-grad and AMC-2′ cells realize opposing reflection phases, and the two unit-cell types over a cavity's aperture should be sufficient to design a low RCS antenna. Besides, if the appearance of a distinct interface of destructive interference is ignored in one of the principal axes, it is likely that an even smaller size of the cavity's aperture can be realized, compared to Ant-1.

Considering the above, one possible design of Ant-2 was shown in Fig 19, which realized an asymmetric macroscopic layout of the unit-cells for orthogonal polarizations of the incident wave. Such an implementation follows from an example AMC implementation reported in [34]. From Fig. 19, the distinct interface of destructive interference appears along x-axis; whereas, it is non-existent in the y-axis. That is the reason the RCS results of Fig. 23 are non-identical for the VP and HP wave incidences; a notable drawback over Ant-1 design. From Fig. 19(b) and Fig. 19(c), the central FSS-grad part has a 6 × 4 configuration, while the AMC-2′ cells lie in a 6 × 2 configuration, located

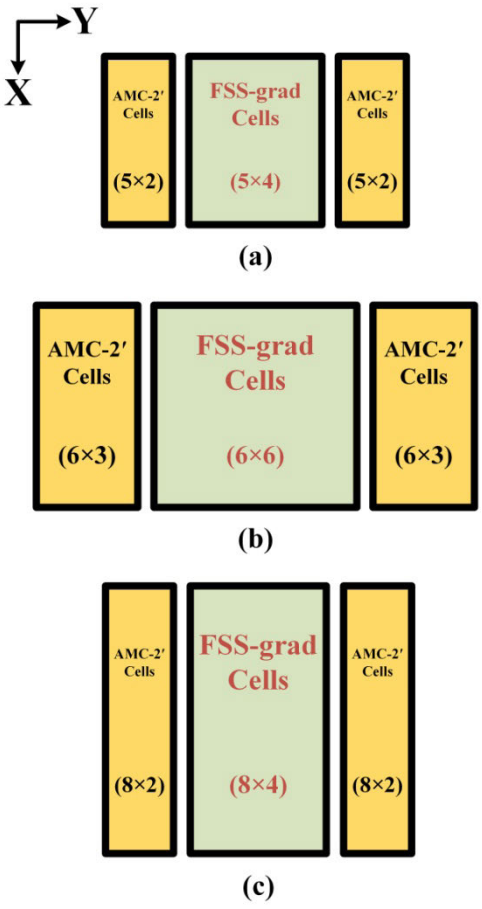

FIGURE 27. Example scenarios of cavity aperture sizes of Ant-2. (a) 5 × 8 unit-cell configuration. (b) 6 × 12 unit-cell configuration. (c) 8 × 8 unit-cell configuration.

laterally to the right and left sides of FSS-grad cells. Here, the adopted configuration of FSS-grad cells has six A'_V values, which are sufficient to easily realize the phase gradation for deflected beam radiation. The surface area occupied by FSS-grad cells is equal to the total surface area occupied by AMC-2′ cells. Again, this is necessary to achieve proper phase cancellation of the reflected wave from the superstrate surface.

So, based on the design of Fig. 19, example variations of the aperture size of Ant-2 are shown in Fig. 27, depicting 5 × 8 unit-cell configuration in Fig. 27(a), 6 × 12 unit cell configuration in Fig. 27(b), and 8 × 8 unit-cell configuration in Fig. 27(c). The common attribute among all scenarios of Fig. 27 is that the surface areas of opposing refection phase unit-cells are equal. Moreover, the said placement of unit-cell elements realizes distinct interface of opposing reflection phase unit-cells only along vertical axis (x-axis).

Among the designs of Fig. 19 and Fig. 27, our choice/preference is the design of Fig. 19, because it offers increased flexibility for gradient implementation (six A'_V values) in comparison to Fig. 27(a), and has a smaller footprint (cavity aperture size) than both Fig. 27(b) and Fig. 27(c).

TABLE 6. Proposed FP antennas (Ant-1 and Ant-2) compared with relevant works.

Ref.	Cavity Dimensions	Center Frequency (GHz)	Gain (dBi)	-10 dB Impedance Bandwidth (MHz)	RCS Reduction Band (GHz)	Average RCS Reduction (dB)	Superstrate Structure	Beam Tilt
[9]	$2.3\lambda \times 2.3\lambda \times 0.58\lambda = 3.07\lambda^3$	11.5	13.2	800 (6.9%)	6-14 (80%)	10	Resistive FSS	0°
[40]	$2.53\lambda \times 2.53\lambda \times 0.67\lambda = 4.29\lambda^3$	7.65	12.3	850 (11.1%)	5-13 (88.8%)	-	Resistive FSS	0°
[11]	$3.7\lambda \times 3.7\lambda \times 0.73\lambda = 9.99\lambda^3$	10	18.4	80 (~1%)	8–17 (72%)	13	Resistive FSS	0°
[10]	$2.79\lambda \times 2.79\lambda \times 0.68\lambda = 5.29\lambda^3$	9.05 – 10 (adaptive)	13.7	variable	7–14 (66.6%)	-	Resistive FSS	0°
[12]	$3.36\lambda \times 3.36\lambda \times 0.7\lambda = 7.9\lambda^3$	8.4	17.9	150 (1.8%)	7–15 (72.7%)	9.9	Resistive FSS	0°
[39]	$2\lambda \times 2\lambda \times 0.47\lambda = 1.88\lambda^3$	10	10.2	1100 (10.8%)	3-15 (133.3%)	>10	Resistive Quasi-Fractal	0°
[41]	$3.67\lambda \times 3.67\lambda \times 0.62\lambda = 8.35\lambda^3$	10	19.8	210 (2.1%)	8–12 (40%)	8.76	Coding Metasurface	0°
[15]	$2.2\lambda \times 2.2\lambda \times 0.52\lambda = 2.52\lambda^3$	10.4	~12	1880 (18.1%)	8-18 (76.9%)	-	AMC	0°
[14]	$2.93\lambda \times 2.93\lambda \times 0.51\lambda = 4.38\lambda^3$	9.6	13.2	~800 (8.4%)	8-14 (54.5%)	-	AMC	0°
[25]	$2.11\lambda \times 2.11\lambda \times 0.44\lambda = 1.96\lambda^3$	6.6	11.5	240 (3.6%)	5.6-16 (96.3%)	13	Resistive FSS + Phase Gradated PRS	-13°
[26]	$2.1\lambda \times 2.1\lambda \times 0.26\lambda = 1.15\lambda^3$	6	9.4	443 (7.3%)	4-16 (120%)	8.5	Resistive FSS + Phase Gradated PRS	-38°
Ant-1	$2.73\lambda \times 2.73\lambda \times 0.33\lambda = 2.46\lambda^3$	7	12	600 (8.3%)	4-13 (105.8%)	12.2	AMC + Phase Gradated FSS	-60°
Ant-2	$1.82\lambda \times 2.42\lambda \times 0.30\lambda = 1.32\lambda^3$	7	11.73	160 (2.3%)	4-13 (105.8% VP) 5.2-13 (85.7% HP)	12.36 (VP) 11.56 (HP)	AMC + Phase Gradated FSS	-37°

VII. DISCUSSION AND COMPARISON OF Ant-1 AND Ant-2 WITH PREVIOUS WORKS

To establish the significance of the proposed work, it is compared with other low RCS FP antenna designs from the literature, as highlighted in Table 6. It can be seen that over all other antennas except [26] and [39], Ant-1 in its both polarizations, and Ant-2 in its vertical polarization, achieve the widest RCS reduction bandwidth of 105.8%. Ant-2 in the horizontal polarization achieves 85.7% of RCS reduction bandwidth, which is higher than most of the works. Except [26], the FP cavity height of both proposed antennas is also smaller when compared to other references, and is only 0.33λ for Ant-1, and 0.3λ for Ant-2. Likewise, since the RCS reduction is based on AMC technology, no RF resistors have been employed, in contrast to the works in [9]–[12], [25], [26], [39], [40], which employ a large number of resistors, and hence pose fabrication complexity.

The -10 dB impedance bandwidth of Ant-1 is comparable to [14], while it is lower than [15], [39], and [40]. However, on the other hand, the RCS reduction bandwidth as well as cavity dimensions of [40] are inferior to Ant-1; the proposed quasi-fractal unit-cell structure of [39] is difficult to fabricate; and the unit-cell design of [15] has been particularly devised for wide bandwidth- by realizing positive gradient of the reflection phase of its PRS. The impedance bandwidth of Ant-2 is somewhat lower; nevertheless, it is still better than the previous works reported in [11], [12], and [41].

The achieved gain for both proposed designs is higher than [26] and [39], and comparable to [15], [25], and [40], while other designs have higher radiated gains. This is because the peak radiation of the proposed designs is deflected off-broadside, and hence this beam tilt is the cause of the lower gain value. In other words, the inferior gain is because of the scan loss [42]. Moreover, mainly because of the relative lower gain values, the aperture efficiencies of the proposed designs are also somewhat on the lower side. The aperture efficiency of Ant-1 is about 17%, while that of Ant-2 is 27%. Finally, both proposed antennas can achieve radiation beam tilt, which is $-60°$ for Ant-1, and $-37°$ for Ant-2. The low RCS antennas presented in [25] and [26] also realize a tilted beam operation; nevertheless, the superstrate structures of the proposed antennas are different, in that, the realization of low RCS and tilted beam functionality is based on the integration of phase gradient metasurface within the AMC based design. The advantage over [25] and [26] is the reduction of fabrication cost and complexity, as no more resistors are required on the superstrate surface. Furthermore, it also avoids the loss incurred to the radiated wave as a result of attenuation within the resistors [12]. This can broadly be validated by the fact that the radiation efficiencies of both Ant-1 and Ant-2 are higher in comparison to the designs reported in [25] and [26]. For [25] and [26], which also consist of two layer (dielectric) superstructure design, and made of similar dielectric as of this work, their radiation efficiencies

are 79% and 60%, respectively. The radiation efficiency of Ant-1 is 84%, and that of Ant-2 is 86%.

The primary advantage of Ant-2 over Ant-1 lies in its design, in that, it is less complex than Ant-1 as it employs two different unit-cells to achieve RCS reduction. This makes its aperture size 41% smaller than Ant-1 to achieve similar RCS reduction for at least one polarization of the incident wave. However, on the other hand, a better advantage of Ant-1 over Ant-2 is its macroscopic symmetric layout, by virtue of which identical RCS frequency and angular response is obtained for arbitrary polarizations. This feature is deemed to be of higher practical value, and hence renders the overall performance of Ant-1 superior to Ant-2.

VIII. DESIGN PROCEDURE TO SYNTHESIZE OPTIMIZED GEOMETRICAL PARAMETERS

A step-by-step design procedure to synthesize geometrical parameters of the antenna for achieving an optimized performance are outlined below. The design procedure holds true for both proposed antennas.

1) Start with an identical air gap (g) for all unit-cell designs, and optimize g in parallel with fine tuning other geometrical parameters of the unit-cells.
2) AMC-1 is a single resonance structure (resonance here refers to the frequency at which reflection phase curve crosses zero degree phase). Determine parameter P_{1L} of AMC-1 to achieve desired resonance and slope of the reflection phase curve, as shown in Fig. 4(a).
3) For the FSS-grad response shown in Fig. 4(a), make sure the optimized g value is such that the reflection phase response of FSS-grad (despite the variation of A_V) closely follows the response of AMC-1.
4) AMC-2 is a dual resonance structure, and its resonances are tuned through parameters L_L, L_W and P_{2L}. Determine an optimized set of L_L, L_W and P_{2L} values. While optimizing, make sure the reflection phase cancellation condition ($\Delta = 180° \pm 37°$) between AMC-2 and AMC-1 (where the reflection response of AMC-1 and FSS-grad are almost identical) is satisfied over the widest possible bandwidth, as realized in Fig. 4(a).
5) If desired, some further fine tuning of AMC-1 and AMC-2 reflection phase properties (as of Fig. 4(a)) can be achieved through the parameter A_{PR}. However, its impact will be very small.
6) Tune parameter P_F. This will set the desired resonant frequency at which the phase gradient approach of FSS-grad is to be leveraged to achieve antenna beam tilting operation. At a fixed P_F value, phase gradation for antenna beam deflection will be achieved through varying A_V values, as shown in Fig. 5(b).
7) Assemble the FP cavity antenna in consideration of the unit-cells placement on the cavity's aperture discussed in section VI. A tuned patch antenna will serve as the excitation source of this cavity.
8) Using equation (2), determine the approximate cavity height (h) considering the desired resonant frequency for the FP cavity.
9) Tune A_V values. Also fine tune the cavity height (h) to finally achieve the desired shaped beam at the required resonant frequency.

Steps 1-4 are inter-linked, and may require few back and forth numerical simulations to achieve the purpose.

IX. CONCLUSION

In this work, two FP antennas have been presented, Ant-1 and Ant-2. The design of Ant-1 is based on three unit-cells, AMC-1, AMC-2 and FSS-grad. The three unit-cells have been integrated on the aperture in such a way that RCS reduction, gain enhancement, and tilted beam operation have been realized all simultaneously. Wideband RCS reduction has been achieved for arbitrary polarizations (105.8%). Average RCS reduction is above 12 dB. Simulation and measurement results have been presented for Ant-1. Ant-2 is a modified version of Ant-1, whereby its design is based on Average RCS reduction is above 12 dB. Simulation and measurement results have been presented for Ant-1. Ant-2 is a modified version of Ant-1, whereby its design is based on two unit-cells, AMC-2′ and FSS-grad. AMC-2′ has been derived from AMC-2 of Ant-1, by doing slight alterations. The aperture size of Ant-2 is smaller than Ant-1. Cavity height is also slightly less than that of Ant-1. The layout of unit-cells on the aperture of Ant-2 is asymmetric; therefore, there is a 20.1% difference of RCS reduction bandwidth between the arbitrary polarizations. For the HP wave, it is again 105.8%. For VP wave case, it is 85.7%; nevertheless, it is still wide enough in comparison to the previous works. Ant-2 also achieves gain enhancement and tilted beam operation. Simulations have been presented for Ant-2. Comparing Ant-1 and Ant-2 to previous works, RCS reduction bandwidth is better than most of the works. Moreover, the achievement of low RCS as well as radiation peak deflection, achieved through the integration of phase gradient metasurface within the AMC based design, has not been realized previously. The proposed antennas, in general, can be useful for any stealth type (low RCS) military application where fixed tilt angle radiators are desired for communication. It is intended to consider the implementation of the proposed antennas with circular polarization (CP) as a future extension of this work.

REFERENCES

[1] C. B. Wilsen and D. B. Davidson, "The radar cross section reduction of microstrip patches," in *Proc. IEEE. AFRICON*, Dec. 1996, pp. 730–733.
[2] W. Wiesbeck and E. Heidrich, "Influence of antennas on the radar cross section of camouflaged aircraft," in *Proc. Int. Conf. Radar*, Oct. 1992, pp. 122–125.
[3] C. L. Holloway, E. F. Kuester, J. A. Gordon, J. O'Hara, J. Booth, and D. R. Smith, "An overview of the theory and applications of metasurfaces: The two-dimensional equivalents of metamaterials," *IEEE Antennas Propag. Mag.*, vol. 54, no. 2, pp. 10–35, Apr. 2012.
[4] F. Costa and A. Monorchio, "A frequency selective radome with wideband absorbing properties," *IEEE Trans. Antennas Propag.*, vol. 60, no. 6, pp. 2740–2747, Jun. 2012.

[5] S. Genovesi, F. Costa, and A. Monorchio, "Low-profile array with reduced radar cross section by using hybrid frequency selective surfaces," *IEEE Trans. Antennas Propag.*, vol. 60, no. 5, pp. 2327–2335, May 2012.
[6] Q. Gao, Y. Yin, D.-B. Yan, and N. C. Yuan, "Application of metamaterials to ultra-thin radar-absorbing material design," *Electron. Lett.*, vol. 41, no. 17, pp. 936–937, Aug. 2005.
[7] Y. Liu and X. Zhao, "Perfect absorber metamaterial for designing low-RCS patch antenna," *IEEE Antennas Wireless Propag. Lett.*, vol. 13, pp. 1473–1476, 2014.
[8] S. Li, J. Gao, X. Cao, Y. Zhao, Z. Zhang, and H. Liu, "Loading metamaterial perfect absorber method for in-band radar cross section reduction based on the surface current distribution of array antennas," *IET Microw., Antennas Propag.*, vol. 9, no. 5, pp. 399–406, Apr. 2015.
[9] W. Pan, C. Huang, P. Chen, X. Ma, C. Hu, and X. Luo, "A low-RCS and high-gain partially reflecting surface antenna," *IEEE Trans. Antennas Propag.*, vol. 62, no. 2, pp. 945–949, Feb. 2014.
[10] C. Huang, W. Pan, X. Ma, and X. Luo, "A frequency reconfigurable directive antenna with wideband low-RCS property," *IEEE Trans. Antennas Propag.*, vol. 64, no. 3, pp. 1173–1178, Mar. 2016.
[11] H. Jiang, Z. Xue, W. Li, W. Ren, and M. Cao, "Low-RCS high-gain partially reflecting surface antenna with metamaterial ground plane," *IEEE Trans. Antennas Propag.*, vol. 64, no. 9, pp. 4127–4132, Sep. 2016.
[12] Y. Jia, Y. Liu, W. Zhang, J. Wang, S. Gong, and G. Liao, "High-gain Fabry–Perot antennas with wideband low monostatic RCS using phase gradient metasurface," *IEEE Access*, vol. 7, pp. 4816–4824, 2019.
[13] F. Costa, A. Monorchio, and G. Manara, "Analysis and design of ultra thin electromagnetic absorbers comprising resistively loaded high impedance surfaces," *IEEE Trans. Antennas Propag.*, vol. 58, no. 5, pp. 1551–1558, May 2010.
[14] Y.-J. Zheng, J. Gao, X.-Y. Cao, S.-J. Li, and W.-Q. Li, "Wideband RCS reduction and gain enhancement microstrip antenna using chessboard configuration superstrate," *Microw. Opt. Technol. Lett.*, vol. 57, no. 7, pp. 1738–1741, Jul. 2015.
[15] Y. Zheng, J. Gao, Y. Zhou, X. Cao, H. Yang, S. Li, and T. Li, "Wideband gain enhancement and RCS reduction of Fabry–Perot resonator antenna with chessboard arranged metamaterial superstrate," *IEEE Trans. Antennas Propag.*, vol. 66, no. 2, pp. 590–599, Feb. 2018.
[16] J. C. I. Galarregui, A. T. Pereda, J. L. M. D. Falcon, I. Ederra, R. Gonzalo, and P. D. Maagt, "Broadband radar cross-section reduction using AMC technology," *IEEE Trans. Antennas Propag.*, vol. 61, no. 12, pp. 6136–6143, Dec. 2013.
[17] Y. Zheng, J. Gao, X. Cao, Z. Yuan, and H. Yang, "Wideband RCS reduction of a microstrip antenna using artificial magnetic conductor structures," *IEEE Antennas Wireless Propag. Lett.*, vol. 14, pp. 1582–1585, 2015.
[18] S. Zarbakhsh, M. Akbari, F. Samadi, and A.-R. Sebak, "Broadband and high-gain circularly-polarized antenna with low RCS," *IEEE Trans. Antennas Propag.*, vol. 67, no. 1, pp. 16–23, Jan. 2019.
[19] H. Nakano, Y. Ogino, and J. Yamauchi, "Bent two-leaf antenna radiating a tilted, linearly polarized, wide beam," *IEEE Trans. Antennas Propag.*, vol. 58, no. 11, pp. 3721–3725, Nov. 2010.
[20] A. Dadgarpour, B. Zarghooni, B. S. Virdee, and T. A. Denidni, "Beam tilting antenna using integrated metamaterial loading," *IEEE Trans. Antennas Propag.*, vol. 62, no. 5, pp. 2874–2879, May 2014.
[21] J. Yu, W.-J. Lu, Y. Cheng, and L. Zhu, "Tilted circularly polarized beam microstrip antenna with miniaturized circular sector patch under wideband dual-mode resonance," *IEEE Trans. Antennas Propag.*, vol. 68, no. 9, pp. 6580–6590, Sep. 2020.
[22] A. Ourir, S. Burokur, and A. D. Lustrac, "Phase-varying metamaterial for compact steerable directive antennas," *Electron. Lett.*, vol. 43, no. 9, pp. 493–494, 2007.
[23] H. Nakano, S. Mitsui, and J. Yamauchi, "Tilted-beam high gain antenna system composed of a patch antenna and periodically arrayed loops," *IEEE Trans. Antennas Propag.*, vol. 62, no. 6, pp. 2917–2925, Jun. 2014.
[24] F. Qin, S. Gao, C. Mao, G. Wei, J. Xu, and J. Li, "Low-profile high-gain tilted-beam Fabry–Perot antenna," in *Proc. 9th Eur. Conf. Antennas Propag. (EuCAP)*, Apr. 2015, pp. 1–5.
[25] H. Umair, T. B. A. Latef, Y. Yamada, W. N. L. B. W. Mahadi, M. Othman, K. Kamardin, M. I. Hussein, and A. I. Najam, "Tilted beam Fabry–Perot antenna with enhanced gain and broadband low backscattering," *Electronics*, vol. 10, no. 3, p. 267, Jan. 2021.
[26] H. Umair, T. B. A. Latef, Y. Yamada, T. Hassan, W. N. L. B. W. Mahadi, M. Othman, K. Kamardin, and M. I. Hussein, "Quarter wavelength Fabry–Perot cavity antenna with wideband low monostatic radar cross section and off-broadside peak radiation," *Appl. Sci.*, vol. 11, no. 3, p. 1053, Jan. 2021.
[27] J. T. S. Sumantyo, "Design of tilted beam circularly polarized antenna for CP-SAR sensor onboard UAV," in *Proc. Int. Symp. Antennas Propag. (ISAP)*, Oct. 2016, pp. 658–659.
[28] T. Hassan, M. U. Khan, H. Attia, and M. S. Sharawi, "An FSS based correlation reduction technique for MIMO antennas," *IEEE Trans. Antennas Propag.*, vol. 66, no. 9, pp. 4900–4905, Sep. 2018.
[29] M. Paquay, J.-C. Iriarte, I. Ederra, R. Gonzalo, and P. de Maagt, "Thin AMC structure for radar cross-section reduction," *IEEE Trans. Antennas Propag.*, vol. 55, no. 12, pp. 3630–3638, Dec. 2007.
[30] W. Chen, C. A. Balanis, and C. R. Birtcher, "Checkerboard EBG surfaces for wideband radar cross section reduction," *IEEE Trans. Antennas Propag.*, vol. 63, no. 6, pp. 2636–2645, Jun. 2015.
[31] A. Y. Modi, C. A. Balanis, C. R. Birtcher, and H. N. Shaman, "Novel design of ultrabroadband radar cross section reduction surfaces using artificial magnetic conductors," *IEEE Trans. Antennas Propag.*, vol. 65, no. 10, pp. 5406–5417, Oct. 2017.
[32] Y. Zheng, J. Gao, L. Xu, X. Cao, and T. Liu, "Ultrawideband and polarization-independent radar-cross-sectional reduction with composite artificial magnetic conductor surface," *IEEE Antennas Wireless Propag. Lett.*, vol. 16, pp. 1651–1654, 2017.
[33] B. Ratni, W. A. Merzouk, A. D. Lustrac, S. Villers, G.-P. Piau, and S. N. Burokur, "Design of phase-modulated metasurfaces for beam steering in Fabry–Perot cavity antennas," *IEEE Antennas Wireless Propag. Lett.*, vol. 16, pp. 1401–1404, 2017.
[34] Y. Zhao, X. Cao, J. Gao, X. Yao, T. Liu, W. Li, and S. Li, "Broadband low-RCS metasurface and its application on antenna," *IEEE Trans. Antennas Propag.*, vol. 64, no. 7, pp. 2954–2962, Jul. 2016.
[35] A. Foroozesh and L. Shafai, "Investigation into the effects of the patch-type FSS superstrate on the high-gain cavity resonance antenna design," *IEEE Trans. Antennas Propag.*, vol. 58, no. 2, pp. 258–270, Feb. 2010.
[36] L.-Y. Ji, Y. J. Guo, P.-Y. Qin, S.-X. Gong, and R. Mittra, "A reconfigurable partially reflective surface (PRS) antenna for beam steering," *IEEE Trans. Antennas Propag.*, vol. 63, no. 6, pp. 2387–2395, Jun. 2015.
[37] N. Wang, Q. Liu, C. Wu, L. Talbi, Q. Zeng, and J. Xu, "Wideband Fabry–Perot resonator antenna with two complementary FSS layers," *IEEE Trans. Antennas Propag.*, vol. 62, no. 5, pp. 2463–2471, May 2014.
[38] S. N. Burokur, R. Yahiaoui, and A. de Lustrac, "Subwavelength metamaterial-based resonant cavities fed by multiple sources for high directivity," *Microw. Opt. Technol. Lett.*, vol. 51, no. 8, pp. 1883–1888, Aug. 2009.
[39] W. Li, X. Cao, J. Gao, Z. Zhang, and L. Cong, "Broadband RCS reduction and gain enhancement microstrip antenna using shared aperture artificial composite material based on quasi-fractal tree," *IET Microw., Antennas Propag.*, vol. 10, no. 4, pp. 370–377, Mar. 2016.
[40] J. Mu, H. Wang, H. Wang, and Y. Huang, "Low-RCS and gain enhancement design of a novel partially reflecting and absorbing surface antenna," *IEEE Antennas Wireless Propag. Lett.*, vol. 16, pp. 1903–1906, 2017.
[41] L. Zhang, X. Wan, S. Liu, J. Y. Yin, Q. Zhang, H. T. Wu, and T. J. Cui, "Realization of low scattering for a high-gain Fabry–Perot antenna using coding metasurface," *IEEE Trans. Antennas Propag.*, vol. 65, no. 7, pp. 3374–3383, Jul. 2017.
[42] R. J. Mailloux, *Phased Array Antenna Handbook*. Norwood, MA, USA: Artech House, 2017.

HASSAN UMAIR received the B.E. and M.S. degrees in electrical (telecommunication) engineering from the National University of Sciences and Technology (NUST), Pakistan, in 2010 and 2015, respectively. He is currently pursuing the Ph.D. degree in electrical engineering with the University of Malaya (UM), Malaysia.

In 2015, he has served as a visiting faculty for a term in the Electrical Engineering Department, NUST. Later, he joined the National Electronics Complex of Pakistan (NECOP) as a Design Engineer. His research interests include electronic beam steering, dielectric resonator antennas, RFID tag antennas, frequency selective surfaces, and metasurface based radar cross section reduction techniques.

TARIK BIN ABDUL LATEF received the B.Sc. degree in electrical and electronic engineering from the University of Oita, Japan, in 1997, the M.Sc. degree in electrical engineering from the University of Leeds, and the Ph.D. degree from The University of Sheffield, U.K., in 2005 and 2011, respectively.

Since 2011, he has been a Senior Lecturer with the Department of Electrical Engineering, Faculty of Engineering, University of Malaya, Malaysia. His research interests include circularly polarized antennas, conformal antennas, frequency independent antennas, array design, dielectric resonator antennas, superconducting metamaterial antennas, and RCS reduction mechanisms.

YOSHIHIDE YAMADA received the B.E. and M.E. degrees in electronics from the Nagoya Institute of Technology, Nagoya, Japan, in 1971 and 1973, respectively, and the D.E. degree in electrical engineering from the Tokyo Institute of Technology, Tokyo, Japan, in 1989.

In 1973, he joined the Electrical Communication Laboratory, Nippon Telegraph and Telephone Corporation (NTT). Until 1984, he was involved in research and development of reflector antennas for terrestrial and satellite communications. From 1985 to 1993, he was involved on research and development of base station antennas for mobile radio systems. In 1993, he moved to NTT Mobile Communications Network Inc. (NTT DoCoMo). In 1995, he was temporarily transferred to YRP Mobile Telecommunications Key Technology Research Laboratories Company Ltd. He was a Guest Professor with the Cooperative Research Center, Niigata University, and a Lecturer with the Tokyo University of Science, from 1996 to1997. In 1998, he became a Professor at the National Defense Academy, Japan. Since 2014, he has been a Professor with the Malaysia-Japan International Institute of Technology, Universiti Teknologi Malaysia, Kuala Lumpur, Malaysia. His current research interests include very small antennas, array antennas, aperture antennas, and electromagnetic simulation of RCS. He is also a Fellow Member of IEICE and a Senior Member of the IEEE AP Society. He is also a member of ACES. He received the Best Paper Award and the Best Tutorial Paper Award from the IEICE in 2013 and 2014, respectively.

TAYYAB HASSAN received the bachelor's degree in electrical engineering (communications major) and the master's degree in electrical engineering (RF and microwave major) from the National University of Sciences and Technology (NUST), Islamabad, Pakistan, in 2010 and 2018, respectively.

Since December 2011, he has been working with CESAT, Islamabad, where he is currently involved in the design, development, and testing of various kinds of antennas. His research interests include antenna design, electronic beam steering/phased arrays, artificially engineered surfaces, materials measurements, and application of additive manufacturing techniques in RF and Microwave domain.

WAN NOR LIZA BINTI WAN MAHADI was born in Kuala Terengganu, Malaysia. She received the B.E. degree (Hons.) in electrical and electronics from the University of Wales, U.K, and the Ph.D. degree in electrical and electromagnetic engineering from the Wolfson Centre for Magnetic Technology, University of Wales, in 1996.

In November 1996, she started working as a Researcher with SIRIM Berhad, Malaysia. In December 1998, she joined the University of Malaya as a Lecturer, where she is currently serving as an Associate Professor for the Electrical Engineering Department. Her research interests include electromagnetic fields and antenna designs.

MOHAMADARIFF OTHMAN received the bachelor's degree in electronic engineering from Multimedia University, Malaysia, in 2006, and the M.Sc. degree in RF and microwave field and the Ph.D. degree in antenna and propagation from Universiti Sains Malaysia (USM), Malaysia, in 2008 and 2015, respectively.

He joined the Department of Electrical Engineering, University of Malaya, Malaysia, as a Senior Lecturer, in 2016, after serving a private university for almost one and half year. His research interests include 5G antennas, dielectric characterization, dielectric resonator antenna design, and antenna design optimization.

KAMILIA KAMARDIN (Senior Member, IEEE) received the B.Eng. degree in electronic (communications) from The University of Sheffield, U.K., in 2004, the M.Sc. degree in information technology (data communications and networking) from Universiti Teknologi Mara (UiTM), Malaysia, in 2007, and the Ph.D. degree in electrical engineering (communications) from Universiti Teknologi Malaysia (UTM), Malaysia, in 2014.

She spent three months at the University of Birmingham, U.K., as a Visiting Ph.D. Student. She has previously served as a Senior Assistant Researcher with the TM Research & Development, Malaysia, for three years. She also serves as a Senior Lecturer for the Department of Electronic Systems Engineering, Malaysia-Japan International Institute of Technology (MJIIT), Universiti Teknologi Malaysia (UTM), Kuala Lumpur, Malaysia. Her research interests include antennas, wireless communication, wearable communication devices, body centric communication, metamaterials, and the Internet of Things (IoT).

MOUSA I. HUSSEIN received the B.Sc. degree from West Virginia Tech, USA, in 1985, and the M.Sc. and Ph.D. degrees from the University of Manitoba, Winnipeg, MB, Canada, in 1992 and 1995, respectively, all in electrical engineering.

From 1995 to 1997, he was with the Research and Development Group, Integrated Engineering Software Inc., Winnipeg, working on developing EM specialized software based on the boundary element method. In 1997, he joined the Faculty of Engineering, Amman University, Amman, Jordan, as an Assistant Professor. He is currently an Associate Professor with the Electrical Engineering Department, United Arab Emirates University. He has over 70 publications in international journals and conferences. He has supervised several Ph.D. and M.Sc. students. His current research interests include computational electromagnetics, electromagnetic scattering, antenna analysis and design, metamaterial and applications, and material characterization.